15 Sep 2022

Flexural Strength of Innovative Thin-Walled Composite Cold-Formed Steel/PE-ECC Beams

Ahmed Sheta

Xing Ma

Yan Zhuge

Mohamed ElGawady
Missouri University of Science and Technology, elgawadym@mst.edu

et. al. For a complete list of authors, see https://scholarsmine.mst.edu/civarc_enveng_facwork/2281

Recommended Citation

A. Sheta et al., "Flexural Strength of Innovative Thin-Walled Composite Cold-Formed Steel/PE-ECC Beams," *Engineering Structures*, vol. 267, article no. 114675, Elsevier, Sep 2022.
The definitive version is available at https://doi.org/10.1016/j.engstruct.2022.114675

Engineering Structures 267 (2022) 114675

Contents lists available at ScienceDirect

Engineering Structures

journal homepage: www.elsevier.com/locate/engstruct

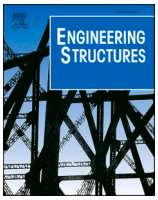

Flexural strength of innovative thin-walled composite cold-formed steel/PE-ECC beams

Ahmed Sheta [a,c], Xing Ma [a,*], Yan Zhuge [a], Mohamed ElGawady [b], Julie Mills [a], Elsayed Abd-Elaal [a,c]

[a] UniSA STEM, University of South Australia, Adelaide, Australia
[b] Department of Civil, Architectural & Environmental Engineering, Missouri University of Science and Technology, MO, USA
[c] Structural Engineering Department, Mansoura University, Mansoura, Egypt

ARTICLE INFO

Keywords:
Composite beams
Flexural strength
CFS
SupaCee
lipped-Cee
PE-ECC
MOR

ABSTRACT

A detailed experimental investigation on the flexural behaviour of an innovative precast composite element combining cold-formed steel (CFS) and engineered cementitious composites (ECC) is presented in this paper. Bonding ECC to the lightweight thin-walled CFS sections enhanced the buckling, bearing, and torsional properties of the composite sections. The proposed composite system will be used as precast flexural members in framed structures with large spans or as a rehabilitation approach for corroded cold-formed and hot-rolled steel flexural members. Simply supported beams with comparatively long spans with span-to-depth ratios of *6.83* and *13.48* were installed back-to-back and tested under a *4*-point loading configuration. The behaviour of composite CFS/ECC beams under bending was investigated and compared with the bare CFS sections. Composite CFS/MOR beams incorporating high-strength mortar (MOR) as an ECC replacement were also investigated. The test specimens were divided into *three* series with *sixteen* tests in total. Series A (SC300) included *six* tests utilising *300-mm* height SupaCee sections, Series B (C300) included *four* tests using *300-mm* height lipped-Cee sections, and Series C (SC150) included *six* tests utilising *150-mm* height SupaCee sections. The composite CFS/ECC beams exhibited high load-bearing capacities after reaching their plastic section capacities, while the bare CFS beams failed to reach their yield section capacities due to distortional buckling. Composite CFS/MOR beams could not reach their plastic moment capacities due to debonding between MOR and CFS after MOR crushing. The moment capacities of the composite CFS/ECC beams increased up to *140.0%* over their duplicate bare CFS sections, while composite CFS/MOR beams showed only a *72.0%* increase over CFS sections. Lastly, design equations to predict the moment capacity of composite CFS/ECC beams are presented, based on the experimental results.

1. Introduction

Thin-walled cold-formed steel (CFS) sections are extensively used in low- to mid-rise constructions as floor joists, bearers, roof purlins, roof trusses, and partition walls due to their superior strength-to-weight ratio, simple manufacturing process, economical transportation and handling, and smooth erection and installation [1]. *Two* shapes of CFS sections, Cee- and Zed-sections in *three* forms: unlipped, lipped, and Supa sections (Fig. 1), are widely used in the construction industry. These sections are fabricated in thicknesses up to *3.2 mm* with different steel grades: *G450*, *G500*, and *G550*. Both Supa and lipped sections are vulnerable to shear, local, distortional, and global buckling as well as web-crippling (bearing) issues at transverse concentrated loading points and supports. The flexural capacities of Supa sections are higher than those of lipped sections due to the existence of the longitudinal web stiffeners and curved lips; however, lipped and Supa sections have identical shear capacities [2]. Optimisation of the cross-sectional shapes of the CFS members could significantly improve their buckling behaviours leading to enhanced ductility, flexural, and energy dissipation capacities [3–5].

Engineered cementitious composite (ECC) is a particular high-ductile concrete that incorporates Polyvinyl Alcohol (PVA) and Polyethylene (PE) fibres, with small fibre volume fractions ($\leq$ *2.0 %*) to achieve high tensile strains ranging from *3.0 %* to *5.0 %* and *8.0 %* to *11.0 %* for PVA- and PE-ECC [6–8]. PVA- and PE-ECC possess tensile-strain capacities equal to *100* to *1000* times those of the traditional concrete strain capacities. The ECC mixtures exhibit multiple micro-cracking under direct

* Corresponding author.
E-mail address: xing.ma@unisa.edu.au (X. Ma).

https://doi.org/10.1016/j.engstruct.2022.114675
Received 9 November 2021; Received in revised form 25 April 2022; Accepted 10 July 2022
Available online 20 July 2022

Nomenclature

Symbol	Definition
λ_c	Slenderness ratio of composite section
λ_{cy}	Slenderness yield limit for composite sections
λ_{cp}	Slenderness plastic limit for composite sections
b_c	Clear width of compression flange of composite section
t_{eq}	Equivalent steel thickness of composite section
n	Modular ratio,$n = E_{CFS}/E_{ECC}$
f_y	CFS yield strength
E_{CFS}	Elastic modulus of CFS
E_{ECC}	Elastic modulus of ECC
M_{cs}	Section moment capacity of composite beam
M_{cy}	Yield moment capacity of composite beam
M_{cp}	Plastic moment capacity of composite beam
$M_{y,CFS}$	Yield moment capacity of CFS section
$M_{cr,ECC}$	Cracking moment capacity of ECC section
$M_{p,CFS}$	Plastic moment capacity of CFS section
$M_{p,ECC}$	Plastic moment capacity of ECC section
Z_f	Full section modulus of CFS section
Z_p	Plastic section modulus of CFS section, ($Z_p = 1.20Z_f$ *for SupaCee* and *lipped-Cee*)
f_c'	Compressive strength of ECC
f_t	Initial cracking strength of ECC
f_{tu}	Ultimate tensile strength of ECC
b	Flange width of ECC section
t	Thickness of ECC section
h	Height of ECC web
h_1	Clear height of ECC web
I_g	Gross moment of inertia of ECC section
y_t	Coordinate of the extreme tensile fibres from the centroid
y_p	Location of plastic neutral axis of ECC section
Z_e	Effective section modulus of CFS sections at yield
Z_c	Effective section modulus of CFS sections at the critical stress (f_c)
f_c	Critical stress in the extreme compression fibres due to distortional buckling
M_D	Design moment capacity of CFS beams
M_c	Critical moment for distortional buckling of CFS beams
M_y	Moment causing initial yield of CFS beam in compression
λ_d	Slenderness ratio of CFS members subjected to distortional buckling
M_{od}	Elastic distortional buckling moment for CFS beams

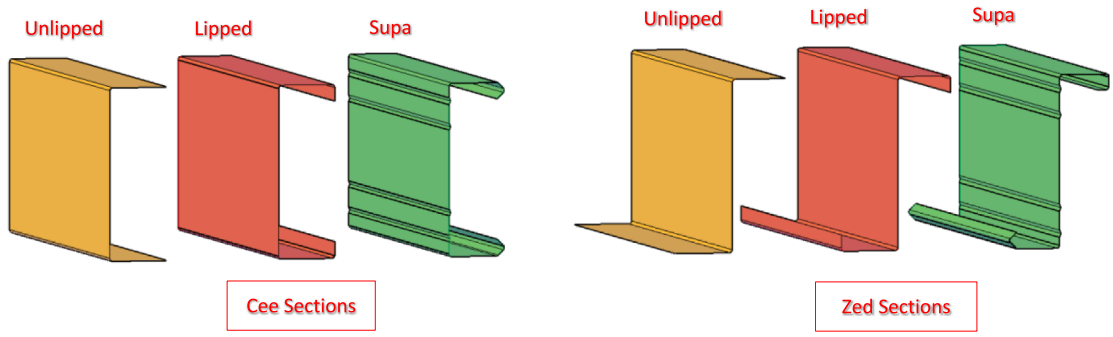

Fig. 1. Cold-formed steel (CFS) sections: Cee and Zed sections.

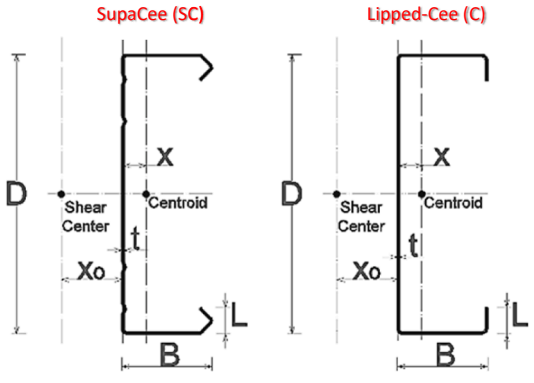

Fig. 2. Cross-section dimensions of SupaCee and lipped-Cee sections.

tension during strain-hardening behaviour with crack widths less than 100.0 μm [9]. Several models were developed to simulate the crack propagation and fracture energy of the fibre-reinforced composites [10,11]. These micro-crack widths make ECC a high-durable construction material compared to traditional concrete [8,12].

Composite members, combining steel and concrete, are broadly utilised in modern constructions, especially in bridges and high-rise buildings [13,14]. The composite steel–concrete members benefit from steel high-strength in tension and concrete high-strength in compression to develop a more effective and economical structural system. Distinct configurations of composite beams utilising hot- and cold-rolled steels and concretes, such as encased beams, partially encased beams, profiled steel sheet beams, and composite steel joists, have been investigated [15–19]. Experimental studies were conducted to investigate the flexural behaviour of conventional reinforced concrete beams utilising cold-formed steel sections to replace tension reinforcement [16,17,20]. The flexural and bond-slip behaviours of encased composite beams comprising high-strength steel sections, lightweight concrete (LWC) and PVA-ECC were investigated. The results revealed that the flexural capacity and overall ductility of the tested beams were improved, compared with bare steel and normal concrete-encased steel beams [18,21–23]. Sheta, Ma [24] investigated experimentally the structural behaviour of a new form of thin-walled composite beams, combining CFS sections and thin layers of ECC. Short- and long-span composite CFS/ECC beams with *three* ECC layer locations: inside, outside, and inside-outside the CFS sections, were studied, and composite beams with the ECC-inside layer exhibited the superior structural performance. Despite the improved behaviour of the new composite beams over the bare CFS beams in terms of strength and ductility, the mixing process

Table 1
Manufacturer's unit weights and dimensions of utilised CFS sections.

Section	SC150		SC300		C300	
	SC15012	SC15024	SC30024	SC30030	C30024	C30030
Type	*SupaCee*	*SupaCee*	*SupaCee*	*SupaCee*	*Lipped-Cee*	*Lipped-Cee*
Weight,*w* [kg/m']	*2.89*	*5.67*	*10.09*	*12.56*	*10.09*	*12.76*
CFS Grade	*G500*	*G450*	*G450*	*G450*	*G450*	*G450*
***t* [mm]**	*1.2*	*2.4*	*2.4*	*3.0*	*2.4*	*3.0*
***D* [mm]**	*152*	*152*	*300*	*300*	*300*	*300*
***B* [mm]**	*60.5*	*63.0*	*99.0*	*100.5*	*96.0*	*96.0*
***L* [mm]**	*18.0*	*20.0*	*28.5*	*29.5*	*27.5*	*31.5*
***x* [mm]**	*17.9*	*18.9*	*25.3*	*25.8*	*25.0*	*25.8*
x_o [mm]	*45.5*	*47.8*	*66.6*	*67.7*	*66.0*	*67.9*

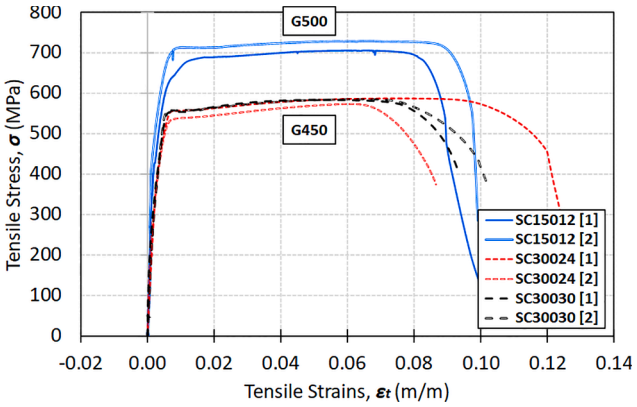

Fig. 3. Stress–strain relations for CFS grades: *G450* and *G500*.

Table 2
Mechanical properties of the Polyethylene (PE) fibres per manufacturer's data.

Property	PE-Fibres
Length (L_f)	*12.0 mm*
Diameter (D_f)	12.0 μm
Length-to-Diameter Ratio (L_f/D_f)	*1000*
Specific Gravity (*SG*)	*1.0 g/cm^3*
Tensile Strength (f_t)	*2.6 GPa*
Tensile Modulus of Elasticity (E_t)	*88.0 GPa*

and cost of the ECC mixtures might limit the broad application of the composite CFS/ECC beams. The innovative composite sections could potentially be used as precast flexural and compression structural elements in large-span framed structures and bridges, with limited buckling and instability issues compared to the common steel members. Moreover, this composite system could be utilised as an economical retrofitting technique for the existing and corroded steel and composite structures.

Although the structural behaviour of the new composite CFS/ECC beams was introduced [24], detailed experimental investigation for flexural and shear behaviours in addition to strength prediction formulas for such beams was lacking. Consequently, this paper presents a detailed experimental study of the flexural behaviour of composite CFS/ECC beams considering the effect of the CFS section's size, thickness, shape and ECC layer's thickness. These composite beams comprise CFS open sections bonded to thin ECC layers without mechanical bonding devices. In this experimental investigation, large-scale beams with span-to-depth (L/d) ratios of *6.83* and *13.67* were tested under *4*-point loading configurations to imitate pure bending conditions. PE-ECC mixture was utilised with *two* typical CFS sections, SupaCee (SC) and lipped-Cee (C) having different sizes and thicknesses in the composite beams. For comparison, a high-strength mortar (MOR) layer was used to replace the PE-ECC layer in *one* composite beam. Finally, flexural strength prediction equations were developed for the proposed composite CFS/ECC sections based on the experimental observations.

2. Experimental scheme

2.1. Material characteristics

2.1.1. Cold-formed steel (CFS) sections

Four SupaCee (SC) sections; SC15012, SC15024, SC30024, and SC30030 and *two* lipped-Cee (C) sections; C30024, and C30030 were used in this experimental investigation. The cross-section geometry and

Fig. 4. Polyethylene (PE) fibres.

Table 3
PE-ECC and MOR mixture proportions (kg/m^3).

Mixture	Cementitious Materials			Aggregates	Water and Admixtures			PE-Fibres	*w/b* [d]
	Cement *(C)*	Slag *(GGBFS)*	Silica Fume *(SF)*	Silica Sand *(SS)*	Water *(W)*	HRWR	VMA		
PE-ECC	*600*	*610*	*115*	*470*	*400*	*15*	*10*	*17.5*	*0.30*
MOR	*600*	*610*	*115*	*470*	*400*	*15*	*10*	——	*0.30*

[d] **.w/b** = W/(C +GGBFS +SF).

Table 4
Mechanical properties of the PE-ECC and MOR mixtures.

Mixture	Air-dry Density, ρ (kg/m^3)	Compressive Strength, $f_c^{'}$ (*MPa*)	Compressive Modulus of Elasticity, E_c (*MPa*)	Splitting Tensile Strength, f_{sp} (*MPa*)	Direct Tensile Behaviour			Flexural Behaviour		
					Ultimate Tensile Strain, ε_{tu} (%)	Initial Cracking Strength, f_t (*MPa*)	Ultimate Tensile Strength, f_{tu} (*MPa*)	Midspan Deflection, Δ (*mm*)	Flexural strength, f_{ft} (*MPa*)	Flexural Toughness, T_b ($kN.mm$)
PE-ECC	1900.0(58.40)	83.40(4.56)	20590.0(1305.0)	8.76(0.63)	8.30(1.20)	3.82(0.37)	7.69(0.62)	27.33(1.20)	16.44(1.77)	29.04(2.43)
MOR	2135.0(63.51)	100.20(5.05)	29850.0(460.0)	4.57(0.36)	0.00644(0.00094)	3.81(0.90)	3.81(0.90)	0.29(0.02)	5.27(0.75)	0.059(0.0011)

Note : The values between parenthesis are the standard deviation (**SD**) of the tested parameters

dimensions per manufacturer's data for the used CFS sections are given in Fig. 2 and Table 1 [25,26]. The initial geometric imperfections of the CFS sections were not measured in this experimental study as their effect might be insignificant in the proposed composite members. However, these imperfections have a substantial effect on the stability of CFS members, subject to interactive buckling modes [27,28].

Two coupons for each thickness: *1.2, 2.4,* and *3.0 mm* were longitudinally extracted from the CFS webs of SC15012, SC30024, and SC30030 to capture their tensile stress–strain behaviour under direct tension per the ASTM E8/E8M [29]. Fig. 3 shows the tensile stress–strain relationships for *G500* (*1.2-mm* thickness) and *G450* (*2.4- & 3.0-mm* thicknesses). For *G450*, the yield strength (f_y) for the test coupons was *490.0 MPa* at a yield strain (ε_y) of *0.0044*, while the ultimate tensile strength (f_u) was *582.0 MPa,* with an ultimate strain (ε_u) of *0.1008*. For *G500,* the yield strength (f_y) was *628.0 MPa* with a yield strain (ε_y) of *0.0052*, while the ultimate tensile strength (f_u) was *717.0 MPa,* with a maximum strain (ε_u) of *0.0944*.

2.1.2. PE-ECC and MOR mixtures

The material ingredients, mixture proportions, and hardened characteristics of the PE-ECC and MOR mixtures are introduced in this section. The mixing techniques, along with the density, particle size distribution, and maximum particle size for the material ingredients, were presented in a previous publication [24]. A PE-ECC mixture with compressive strength ($f_c^{'}$) of *83.40 MPa*, ultimate tensile strength (f_{tu}) of *7.69 MPa* was utilised with CFS sections in the composite beams. A replicate of the ECC mixture without fibres, namely high-strength mortar (MOR), was employed in *one* of the composite beams for comparison with composite beams incorporating ECC.

The mixture proportions for PE-ECC and MOR are presented in Table 3. General-purpose (GP) Portland cement, ground granulated blast furnace slag (GGBFS), and silica fume (SF) [30–32] were incorporated as cementitious materials to enhance the strength and toughness of the PE-ECC and MOR mixtures [8,33,34]. The PE-ECC mixture was reinforced by a *1.75%* total volume fraction of Polyethylene (PE) fibres (Table 2 and Fig. 4**)** with a length-to-diameter ratio of *1000*).

A low water-to-binder ratio, $w/b = 0.30$ was selected for the PE-ECC and MOR mixtures to attain high compressive and tensile strengths. A high-range water reducer (HRWR) and viscosity modifier agent (VMA) were utilised in the mixtures to improve the flowability when pouring the ECC mixtures in narrow thicknesses with a low w/b ratio [35,36].

Table 4 summarises the mechanical characteristics of the hardened PE-ECC and MOR mixtures. The tensile strength vs. tensile strain for PE-ECC and MOR dogbones is presented in Fig. 5**,** while the flexural strength vs. midspan deflection plots of the PE-ECC and MOR flexure beams are shown in Fig. 6. The crack growth in the PE-ECC dogbones and flexure beams can be accurately modelled using finite element (FE) and mesh free models [37,38]. The PE-ECC mixture exhibited superior deformability in tension (Fig. 5(a)) with ultimate tensile strength, $f_{tu} = 7.69 \pm 0.63 MPa$ and ultimate tensile strain, $\varepsilon_{tu} = 8.30 \pm 1.20\%$. On the contrary, MOR displayed low deformability in tension (Fig. 5(b)) with $f_{tu} = 3.81 \pm 0.90 MPa$ and $\varepsilon_{tu} = 0.00644 \pm 0.00094\%$. The tensile strain capacity of the PE-ECC is *1288.0* times that of the MOR and is comparable to the CFS tensile strain. As a result, the PE-ECC mixture is more strain compatible when bonded to the CFS sections than the MOR mixture leading to better composite action between the CFS and PE-ECC. The flexural strengths (f_{ft}) of the PE-ECC and MOR mixtures were $16.44 \pm 1.77 MPa$ and $5.27 \pm 0.75 MPa$ with maximum midspan deflections (Δ) of $27.33 \pm 1.20 mm$ and $0.29 \pm 0.02 mm$, respectively. The flexural toughness (energy dissipation capacity) of the PE-ECC and MOR flexure beams, determined as the area under the load–deflection plots, were $29.04 \pm 2.43 kN.mm$ and $0.059 \pm 0.0011 kN.mm$, respectively.

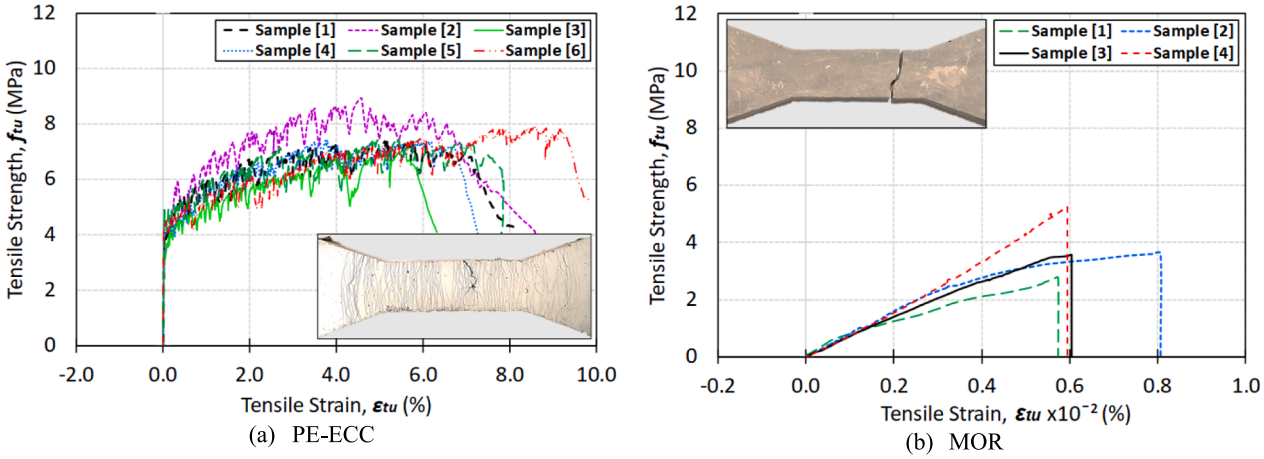

Fig. 5. Behaviour of PE-ECC and MOR dogbones under direct tension.

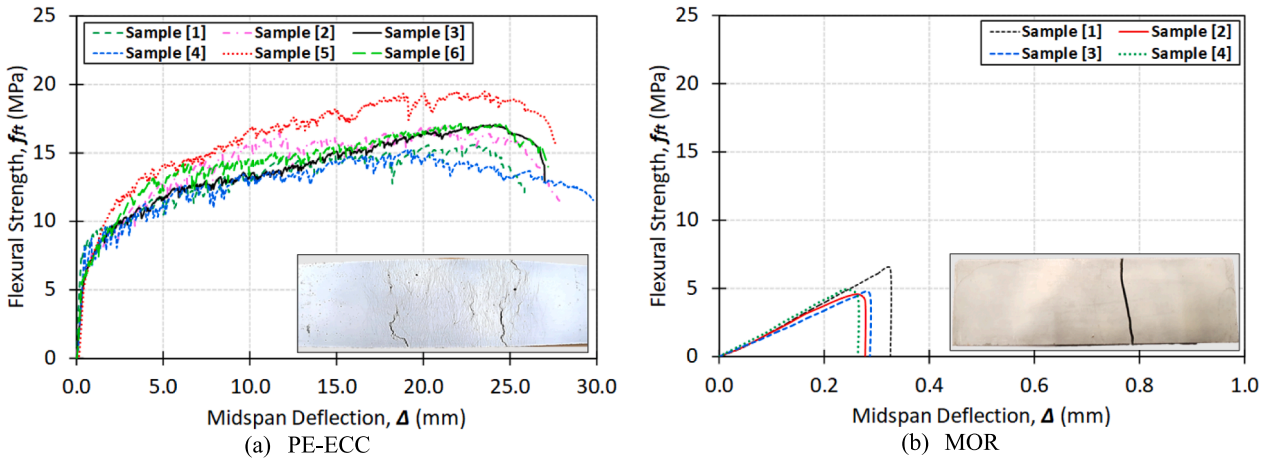

Fig. 6. Behaviour of PE-ECC and MOR beams under flexure.

2.2. Specimens description

The experimental study included sixteen simply supported beams (BM1 to BM16) that were tested under a 4-point loading scheme to investigate the flexural performance of the bare CFS and composite beams. Table 5, Figs. 7 and 8 present the detailed description, dimensions, and cross-section geometry for the tested beams. The tests were conducted on bare CFS and composite CFS/ECC beams with span-to-depth ratios *(L/d)* of *6.83* and *13.48* (where **L** is the span, **d** is the section depth). The flexural strength of the composite CFS/ECC beams is primarily affected by the dimensions, confinement, and interfacial bond between their components: CFS sections and ECC layers. Consequently, this experimental study focused on the size (SC150 & SC300), thickness (*1.2*, *2.4* & *3.0 mm*), shape (SupaCee & lipped-Cee) of the CFS sections and the thickness (*16* & *26 mm*) of the ECC layers. Also, the ECC layer was replaced with the MOR layer in the composite beams to compare their flexural performance.

The tested beams were divided into three Series: Series A (BM1 to BM6) investigated beams utilising SC300 sections, Series B (BM7 to BM10) examined beams utilising C300 sections, and Series C (BM11 to BM16) investigated beams utilising SC150 sections. The tested specimens, excluding BM15 and BM16, consisted of *two* back-to-back bare CFS beams and *two* back-to-back composite beams to resist additional torsional moments. The *two* back-to-back beams were *52.0 mm* apart in Series A and B and separated by *36.0 mm* in Series C, to allow horizontal deformation for both beams. BM15 and BM16, single bare CFS and CFS/ECC sections, were tested to compare the results with those of the back-to-back bare CFS and composite CFS/ECC beams. Series A (SC300) and Series B (C300) incorporated 300-mm height SC- and C-sections with 2.4- and 3.0-mm thicknesses with *two* different ECC thicknesses (16 & 26 *mm*), which were investigated to study the influence of CFS and ECC thicknesses. In addition, BM4 utilised the MOR layer and SC30024 section for comparison with its duplicate composite CFS/ECC beam (BM3). In Series C (SC150), 150-mm height SC-sections with 2.4-mm thickness were employed with a *16-mm* PE-ECC layer in composite CFS/ECC beams.

2.3. Formwork

Fig. 9 shows the details of the formwork used to pour the composite beams in this experimental study. A *1.6-mm* thick steel sheet with was folded into a Cee shape to act as the inner side of the formwork to place the PE-ECC mixtures inside the CFS section. *18-mm* diameter PVC (Polyvinyl Chloride) plastic plugs with lengths of *17.2 mm*, *18.4 mm* and *28.4 mm* were employed to shape the holes in the composite beams and keep the designated PE-ECC and MOR layer thicknesses. *Five* pairs of support angles accompanied with timber stiffeners were utilised to hold the formwork parts together during casting.

2.4. Instrumentation, test configuration, and testing process

A *four*-point loading scheme was adopted to investigate the flexural

Table 5
Test specimen descriptions.

Series	Beam Specimen	Beam Code	Beam Numbering	Span, *L [mm]*	*L/d*	Beam Type	CFS Thickness *[mm]*	ECC/MOR Thickness *[mm]*
Series A [SC300]	SC30024	BM1	BM1 [1] BM1 [2]	*2050.0*	*6.833*	CFS	*2.4*	——
	SC30024-**ECC**16	BM2	BM2 [1] BM2 [2]			Composite CFS/**ECC**		*16.0*
	SC30024-**ECC**26	BM3	BM3 [1] BM3 [2]			Composite CFS/**ECC**		*26.0*
	SC30024-**MOR**26	BM4	BM4 [1] BM4 [2]			Composite CFS/**MOR**		*26.0*
	SC30030	BM5	BM5 [1] BM5 [2]	*2050.0*	*6.833*	CFS	*3.0*	——
	SC30030-**ECC**26	BM6	BM6 [1] BM6 [2]			Composite CFS/**ECC**		*26.0*
Series B [C300]	C30024	BM7	BM7 [1] BM7 [2]	*2050.0*	*6.833*	CFS	*2.4*	——
	C30024-**ECC**26	BM8	BM8 [1] BM8 [2]			Composite CFS/**ECC**		*26.0*
	C30030	BM9	BM9 [1] BM9 [2]	*2050.0*	*6.833*	CFS	*3.0*	——
	C30030-**ECC**26	BM10	BM10 [1] BM10 [2]			Composite CFS/**ECC**		*26.0*
Series C [SC150]	SC15012	BM11	BM11 [1] BM11 [2]	*2050.0*	*13.487*	CFS	*1.2*	——
	SC15012-**ECC**16	BM12	BM12 [1] BM12 [2]			Composite CFS/**ECC**		*16.0*
	SC15024	BM13	BM13 [1] BM13 [2]	*2050.0*	*13.487*	CFS	*2.4*	——
	SC15024-**ECC**16	BM14	BM14 [1] BM14 [2]			Composite CFS/**ECC**		*16.0*
	SC15024-**S**	BM15				CFS		——
	SC15024-**ECC**16-**S**	BM16				Composite CFS/**ECC**		*16.0*

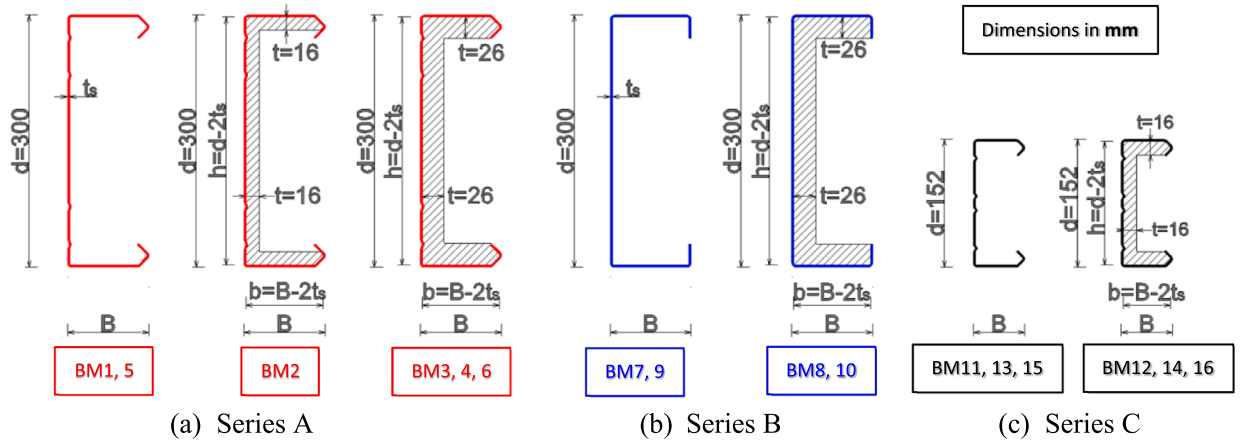

Fig. 7. Test beam cross-sections.

performance of the thin-walled composite CFS/ECC beams, as illustrated in Fig. 10. A displacement control procedure was employed with a *0.5 mm*/min loading rate to apply monotonic loads. Each test comprised *two* horizontally laid beams, bolted back-to-back, separated by a *52-mm* gap in Series A and B and a *36-mm* gap in Series C. The generated gaps were necessary to implement the vertical loads at the beam shear centre to minimise any additional torques (existing when the load is applied away from the shear centre) and to allow independent horizontal deformations for the tested beams. A spreader beam was employed to distribute the vertical loads to the *one-third* span points. Loads were applied at the web of the tested beams through T-stiffeners to avoid top flange curling and bearing failures [2]. Similar T-stiffeners were used as end supports for the tested beams to avoid bearing failure of the bottom flanges. *16-mm* thickness web side plates, with *230.0 mm* height and *100.0 mm* width covering *80.0%* of the CFS section's web height, were attached to each beam at the loading point, and the supports from both sides for Series A, and B. *10-mm* thickness web side plates, with *10.00 mm* height and *100.0 mm* width covering *67.0%* of the CFS section's web height were utilised in Series C. The web side plates dimensions were selected to fit the CFS and composite beam webs. The T-stiffeners and web side plates were essential to avoid any issues related to flange loading, including eccentric loading, web crippling and flange bearing failure at the loading point or the supports [1,39]. The test beams, T-stiffeners and web side plates were assembled using *16 M16* bolts with grade *12.9* in Series A and B and *16 M16* bolts with grade *8.8* in Series C. The bolts arrangement for Series A, B, and C are presented in Fig. 8..

Two linear variable differential transducers (LVDTs) were attached under the beam web at midspan to measure the vertical deformations for both beams (Fig. 10(c)). *Two 5-mm* strain gauges were glued to the top and bottom of the CFS web at midspan (Fig. 9) to capture the maximum compressive and tensile CFS strains under bending. Also, *two 60-mm* strain gauges were attached to the ECC components at similar locations

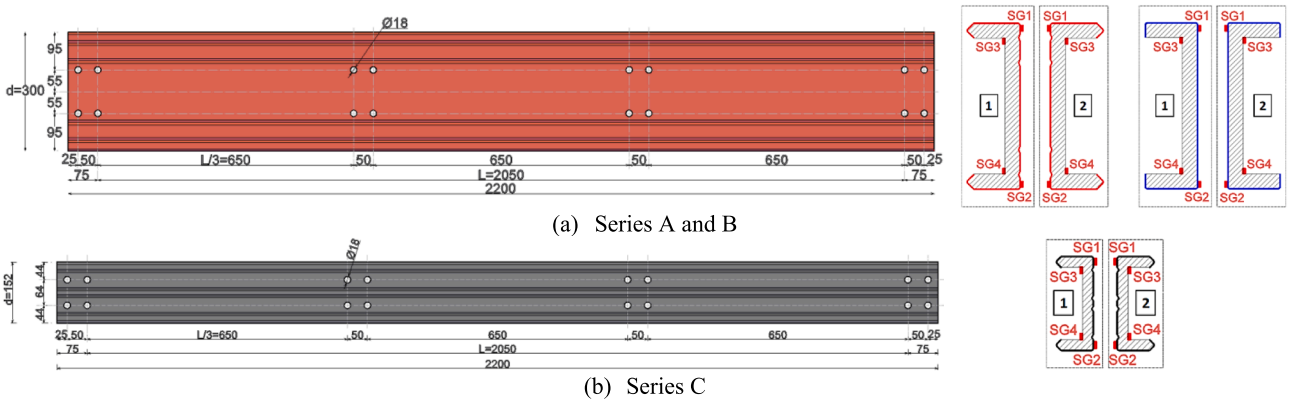

Fig. 8. Dimensions, bolts arrangements and strain gauge locations.

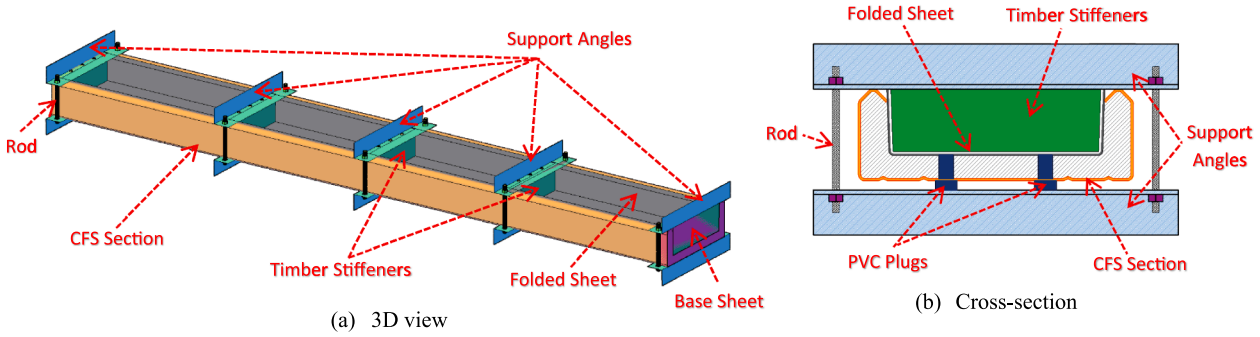

Fig. 9. Formwork details.

(Fig. 9) to measure their maximum compressive and tensile strains.

3. Test results, analysis, and discussion

The moment capacities *(M)*, deflections at midspan *(Δ)*, ductility indices *(μ)*, and flexural toughness *(T_b)* from the experimental study are summarised in Table 6. The comparisons between experimental results for composite beams and their bare CFS beams are shown in Fig. 11. In this study, the yield moment *(M_y)* is defined as the moment at the inception of the beam nonlinear moment-deflection responses (moment-deflection linear region's endpoint) while the peak moment *(M_u)* is the maximum moment applied to the beams. The failure moment *(M_f)* is considered as *70.0%* of the peak moment after degradation.

3.1. Failure modes and moment-deflection responses

The moment vs. midspan deflection for Series A, B and C are presented in Figs. 12-14 while the failure modes are shown in Figs. 15 and 16. The bare CFS beams in Series A, B, and C (BM1, BM5, BM7, BM9, BM11, BM13 & BM15), with different thicknesses and heights, exhibited similar moment-deflection behaviour until failure due to distortional buckling as in Fig. 15(a) & 16(a). The moment linearly increased until buckling initiated in the top flange and web, followed by a nonlinear moment increase until the peak moment. Then, the moment decreased gradually due to distortional buckling failure.

The composite CFS/MOR beam (BM4) exhibited linear moment-deflection behaviour until cracks initiated in the MOR layer around the loading points. A nonlinear moment increase was observed until reaching the peak moment due to the propagation of significant cracks and debonding between the CFS section and the MOR layer. Then, the moment rapidly decreased due to crushing and separation of the MOR layer from the CFS section, followed by buckling of the top flange and web of the CFS section (Fig. 15(c) & 16(d)).

The composite CFS/ECC beams utilising SC-sections with ECC layer filling full lip height (BM3, BM6, BM12 & BM14) exhibited linear moment-deflection behaviours until tensile cracks were initiated around the loading points. Then, nonlinear moment increases were observed with the tensile crack growth until peak moments. Finally, the moment gradually decreased due to significant cracking in the ECC layer until failure due to ECC and CFS rupture at the loading point (Fig. 16(b)). Moreover, BM2 (CFS/ECC beam utilising SC-section with ECC layer filling *60.0%* of CFS lip height) exhibited linear moment-deflection behaviours until tensile cracks were initiated around the loading points. Then, nonlinear moment increases were observed with the tensile crack growth until the peak moment. Finally, the moment gradually decreased due to buckling of the CFS top flange and web, accompanied by cracks in the ECC layer (Fig. 16(b)).

The composite CFS/ECC beams utilising C-sections with ECC layer filling the full CFS lip height (BM8, BM10) exhibited linear moment-deflection behaviours until tensile cracks were initiated around the loading points. Then, nonlinear moment increases were observed with the tensile crack growth until reaching their peak moments. Finally, the moment gradually decreased until failure due to buckling of top flange and web of the CFS sections, followed by crushing of the ECC top flange (Fig. 16(c)).

3.2. Longitudinal strains

The longitudinal strains on the CFS and ECC components for Series A, B, and C are presented in Figs. 17-19. The moment-strain plots show that the composite beams exhibited lower CFS strains at any given moment (up to peak moments) than their bare CFS beams. The ECC layers enhanced the stiffness of CFS sections, leading to higher moment capacities and fewer longitudinal strains (at any specific moment). The

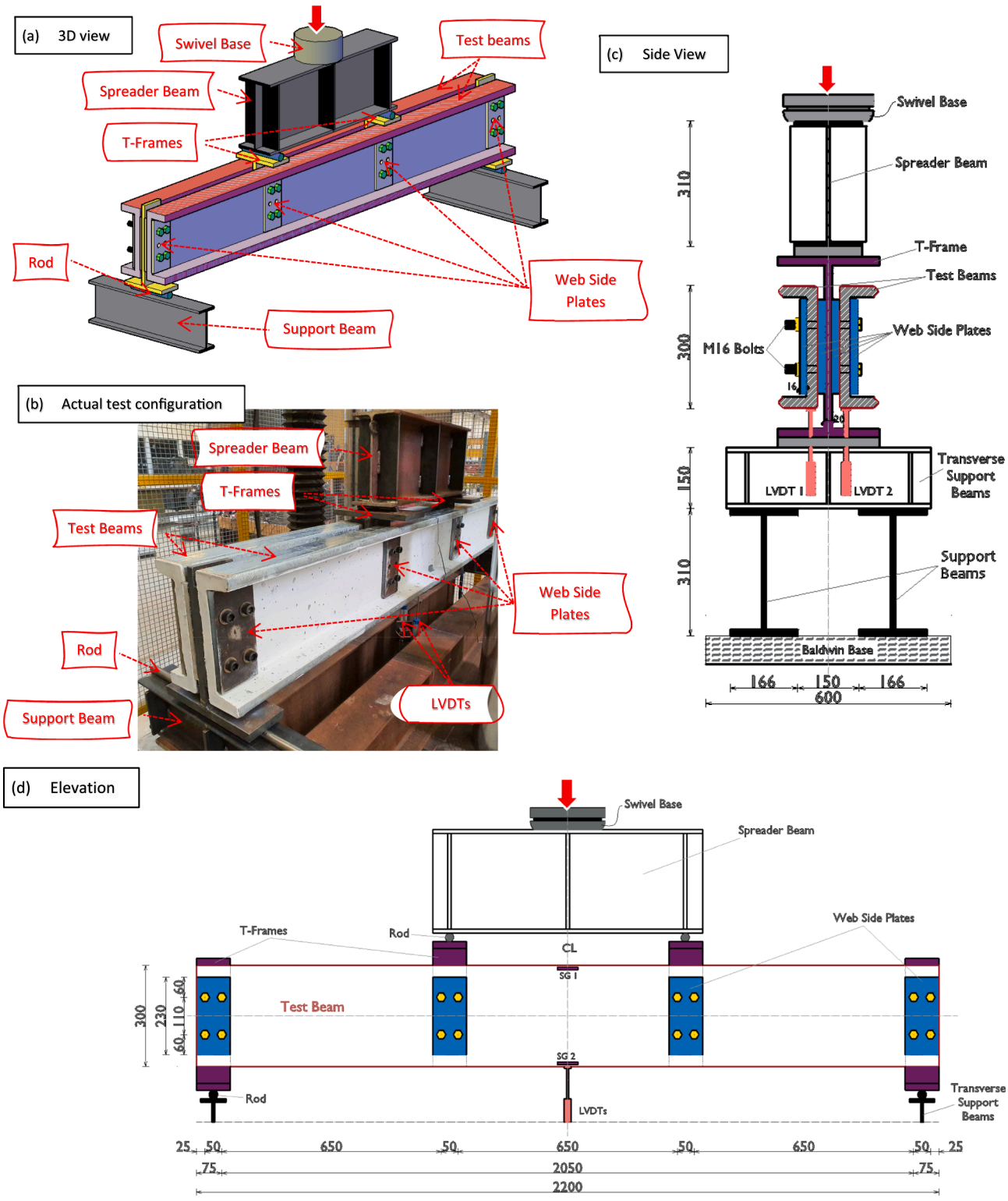

Fig. 10. Test configuration for flexural behaviour of the tested beams.

maximum CFS tensile strains of the composite CFS/ECC beams (with ECC filling full lip height) exceeded the CFS yield strain (ε_y) by *207.0%* on average, ensuring that the composite beams reached their plastic moment capacities.

For Series A, max compressive strains ranging between −3078.0 με and −7380.0 με were recorded on the CFS components, while the max tensile strains ranged between + 2829.0 με and + 8133.0 με. The ECC components exhibited max compressive strains ranging between −1902.0 με and −2456.0 με and max tensile strains ranging between + 5669.0 με and + 6872.0 με. For Series B, the max CFS compressive strains ranged between −2932.0 με and −5575.0 με while the max tensile strains ranged between + 2105.0 με and + 8994.0 με. The max ECC compressive strains ranged between −1722.0 με and −2827.0 με while the max ECC tensile strain for BM8 was + 4962.0 με. For Series C, the max CFS compressive strains fell in the range of −2923.0 με and −4912.0 με while the max tensile strains fell between + 2503.0 με and

Table 6
Moment capacities, midspan deflections, ductility indices, and flexural toughness from the experiments.

Series	Beam Specimen	Beam ID	Yield		Peak		Failure		Failure Mode at Peak Moment	$M_u/M^e_{u,CFS}$	Ductility Index, $\mu = \frac{\Delta_f}{\Delta_y}$	Flexural Toughness, T_b [kN.mm]
			Yield Deflection, Δ_y [mm]	Yield Moment, M_y [kN.m]	Peak Deflection, Δ_p [mm]	Peak Moment, M_u [kN.m]	Failure Deflection, Δ_f [mm]	Failure Moment, M_f [kN.m]				
Series A [SC300]	SC30024	BM1	*12.92*	*33.83*	*16.01*	*37.46*[e]	*20.85*	*26.22*	*-Distortional Buckling of CFS*	*1.00*	*1.614*	*1412*
	SC30024-**ECC**16	BM2	*13.87*	*52.25*	*24.05*	*69.21*	*35.71*	*48.45*	*-Buckling of top flange & web of CFS* *-Tensile cracks in ECC layer*	*1.85*	*2.575*	*4960*
	SC30024-**ECC**26	BM3	*13.91*	*64.54*	*30.40*	*89.66*	*39.95*	*64.95*	*-Local bucking of CFS top flange* *-Rupture of ECC & CFS*	*2.40*	*2.872*	*7718*
	SC30024-**MOR**26	BM4	*10.80*	*43.70*	*20.57*	*64.28*	*32.40*	*44.98*	*-Crushing of MOR* *-Debonding between CFS & MOR* *-Buckling of CFS*	*1.72*	*2.994*	*4346*
	SC30030	BM5	*12.94*	*45.54*	*16.63*	*51.86*[e]	*28.10*	*36.26*	*-Distortional Buckling of CFS*	*1.00*	*2.172*	*2841*
	SC30030-**ECC**26	BM6	*12.60*	*70.94*	*32.42*	*108.25*	*45.34*	*77.73*	*-Local bucking of CFS top flange* *-Rupture of ECC & CFS*	*2.10*	*3.598*	*10,638*
Series B [C300]	C30024	BM7	*11.80*	*31.26*	*15.26*	*35.85*[e]	*20.65*	*25.10*	*-Distortional Buckling of CFS*	*1.00*	*1.750*	*1377*
	C30024-**ECC**26	BM8	*12.64*	*55.77*	*26.10*	*77.56*	*43.39*	*54.30*	*-Buckling of top flange and web of CFS* *-Tensile cracks in ECC bottom flange & crushing of ECC top flange*	*2.16*	*3.433*	*7247*
	C30030	BM9	*11.51*	*47.60*	*14.21*	*54.07*[e]	*26.52*	*37.86*	*-Distortional Buckling of CFS*	*1.00*	*2.304*	*2819*
	C30030-**ECC**26	BM10	*14.17*	*73.42*	*29.63*	*96.75*	*50.19*	*67.74*	*-Buckling of top flange and web of CFS* *-Tensile cracks in ECC bottom flange & crushing of ECC top flange*	*1.80*	*3.542*	*10,987*
Series C [SC150]	SC15012	BM11	*14.00*	*5.71*	*20.78*	*7.81*[e]	*28.30*	*5.79*	*-Distortional Buckling of CFS*	*1.00*	*2.021*	*399*
	SC15012-**ECC**16	BM12	*19.06*	*12.25*	*45.36*	*17.21*	*54.25*	*12.37*	*-Local bucking of CFS top flange* *-Rupture of ECC & CFS*	*2.20*	*2.846*	*1997*
	SC15024	BM13	*21.06*	*14.08*	*32.41*	*17.07*[e]	*39.41*	*11.95*	*-Distortional Buckling of CFS*	*1.00*	*1.871*	*1286*
	SC15024-**ECC**16	BM14	*17.49*	*17.07*	*44.74*	*24.51*	*62.55*	*17.07*	*-Local bucking of CFS top flange* *-Rupture of ECC & CFS*	*1.44*	*3.576*	*3296*
	SC15024-**S**	BM15	*19.14*	*13.16*	*31.70*	*16.91*[e]	*36.08*	*11.85*	*-Distortional Buckling of CFS*	*1.00*	*1.885*	*1131*
	SC15024-**ECC**16-**S**	BM16	*17.59*	*17.11*	*46.59*	*24.21*	*66.79*	*19.17*	*-Local bucking of CFS top flange* *-Rupture of ECC & CFS*	*1.43*	*3.797*	*3709*

[e] $\mathbf{M_{u,CFS}}$ Peak moment capacity of the bare CFS section

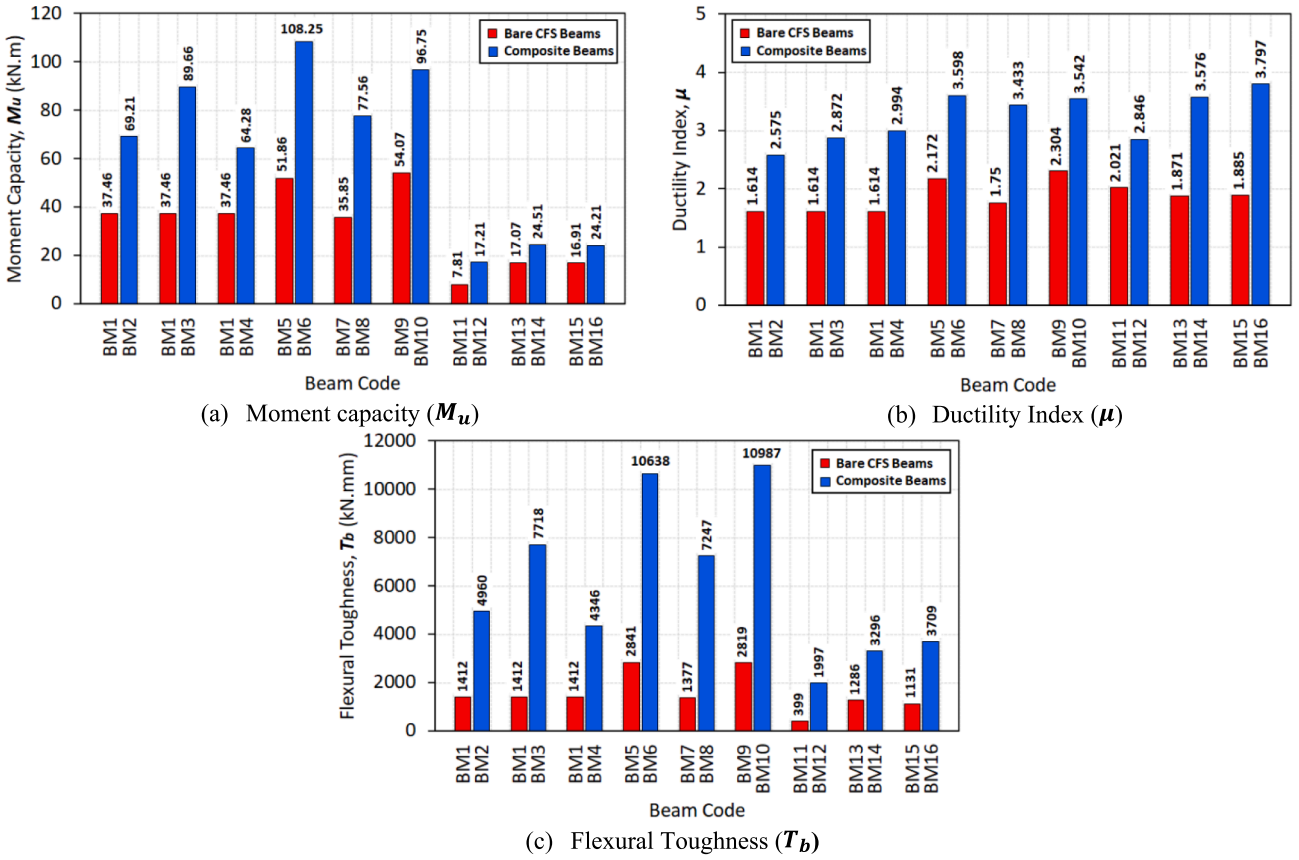

Fig. 11. Comparisons between experimental results for composite beams and their bare CFS beams.

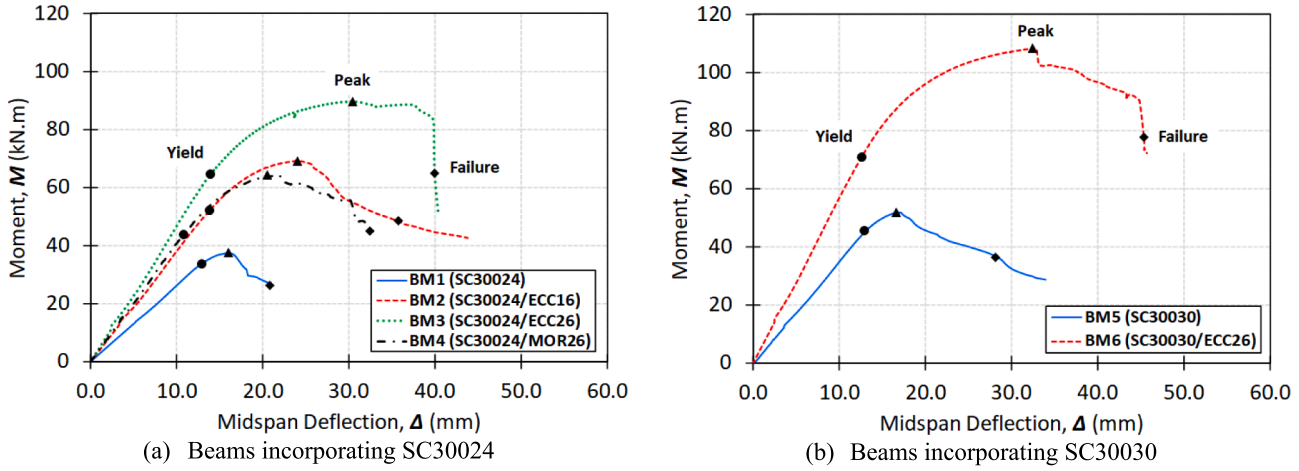

Fig. 12. Moment vs. midspan deflection (Series A).

+ 8517.0 με. Max compressive strains range of −1397.0 με and −1995.0 με and tensile strains range of + 4789.0 με and + 7081.0 με were recorded on the ECC components.

3.3. *Flexural toughness, T_b*

The flexural toughness (T_b) vs. the ultimate moment (M_u) for the tested beams are presented in Fig. 20. The flexural toughness indicates the stored strain energy in the fibre-reinforced mixtures (ECC) and can be defined as the area under the load vs. midspan deflection plots up to failure (*70%* of peak load) [40]. The plots show that the flexural toughness vs. ultimate moment capacities for bare CFS and composite beams follow quite similar trends. The flexural toughness of composite beams was superior compared with their replicate bare CFS beams. In Series A, BM2 (with a *16-mm* ECC layer), BM3 and BM6 (with *26-mm* ECC layers) exhibited flexural toughness increases of *252.0%, 447.0%,* and *275.0%,* respectively over their bare CFS beams (BM1 and BM5). BM4 (with a 26-mm MOR layer) showed a flexural toughness increase of *208.0%*. Similarly in Series B, BM8 and BM10 (with *26-mm* ECC layers) exhibited flexural toughness improvements of *427.0%* and *290.0%* of their bare CFS beams (BM7 and BM9), respectively. For Series C, BM12, BM 14, and BM16 (with *16-mm* ECC layers) displayed flexural toughness increases of *401.0%, 157.0%* and *228.0%* over the bare CFS beams.

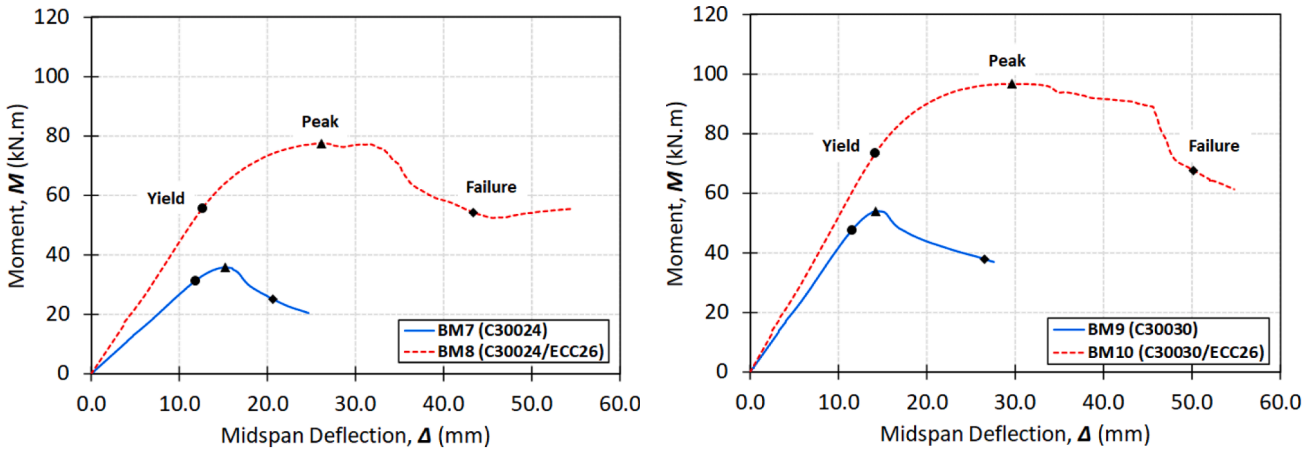

(a) Beams incorporating C30024 (b) Beams incorporating C30030

Fig. 13. Moment vs. midspan deflection (Series B).

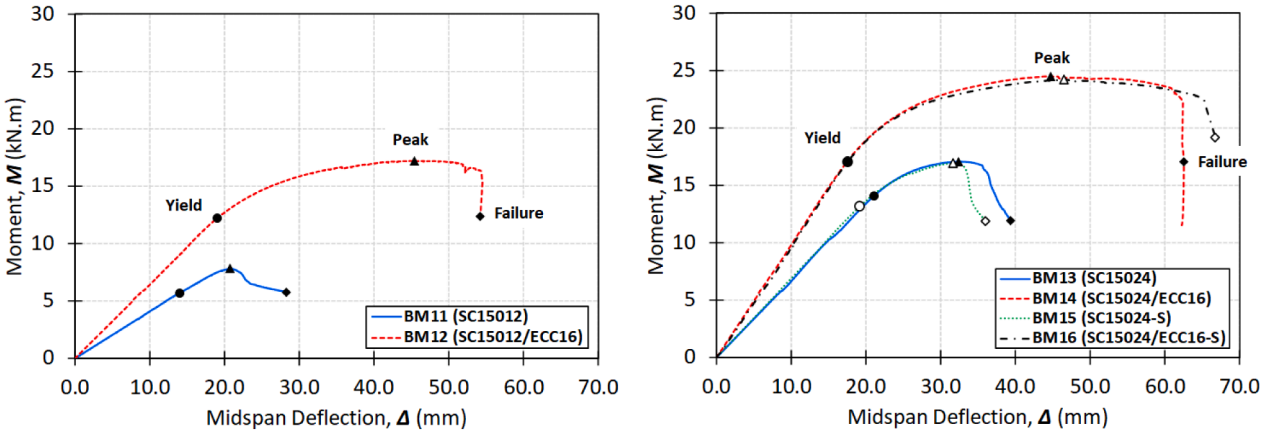

(a) Beams incorporating SC15012 (b) Beams incorporating SC15024

Fig. 14. Moment vs. midspan deflection (Series C).

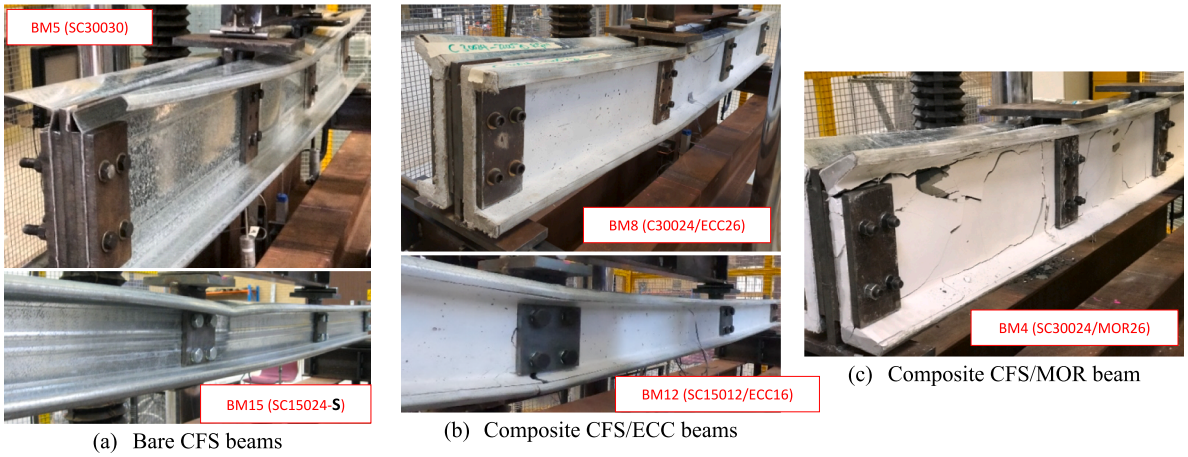

(a) Bare CFS beams (b) Composite CFS/ECC beams (c) Composite CFS/MOR beam

Fig. 15. Overview of CFS, CFS/ECC, CFS/MOR beams after failure.

3.4. Comparison between Series A, B and Series C

The moment vs. midspan deflections and longitudinal strains for Series A (SC300) and B (C300) are compared in Figs. 21 and 22. The bare SupaCee (SC30024 & SC30030) and lipped-Cee (C30024 & C30030) beams exhibited similar flexural performance and failure modes with a slight moment capacity difference of *4.28%* on average. These results indicate that the SC- and C-sections under the prescribed loading conditions possess comparable moment capacities. However, the composite beams incorporating SC-sections showed higher moment capacities over

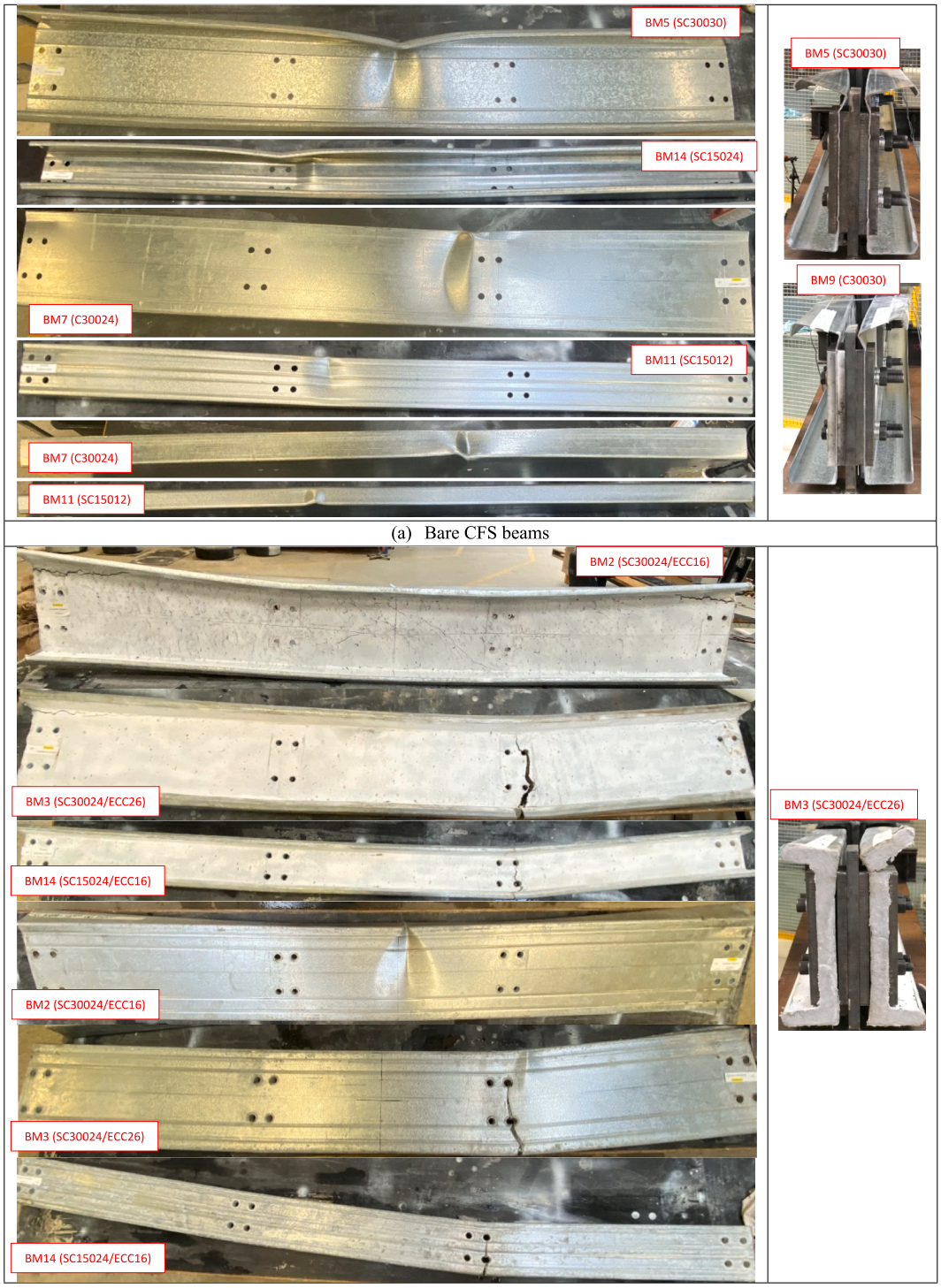

Fig. 16. Failure modes.

their replicates utilising C-sections with a noticeable capacity increase of *13.50%*. The longitudinal strain comparison for composite beams showed that CFS and ECC strains at any specific moment were lower in beams utilising SC-sections. The higher moment capacities, when utilising SC-sections over C-sections in composite CFS/ECC beams, are attributed to the improved confinement of the ECC layer along the top and bottom flanges from the curved lips in SC-sections.

Fig. 23 shows the normalised moment (M/M_{peak}) vs. normalised deflection (Δ/Δ_{peak}) relations for Series A and C. The moment and midspan deflection for each beam were normalised by the peak moment (M_{peak}) and peak deflection (Δ_{peak}). The plots show that the moment-deflection behaviours of bare CFS beams were similar, decreasing after peak moments, regardless of CFS size and thickness. By comparison, the composite CFS/ECC beams with the ECC layer filling the full lip height exhibited identical moment-deflection performances, similar to the plastic steel sections with long plateaus [41], irrespective of the CFS size and thickness. However, the CFS/ECC beam, with the ECC layer filling *60.0%* of the CFS lip height, exhibited moment-deflection

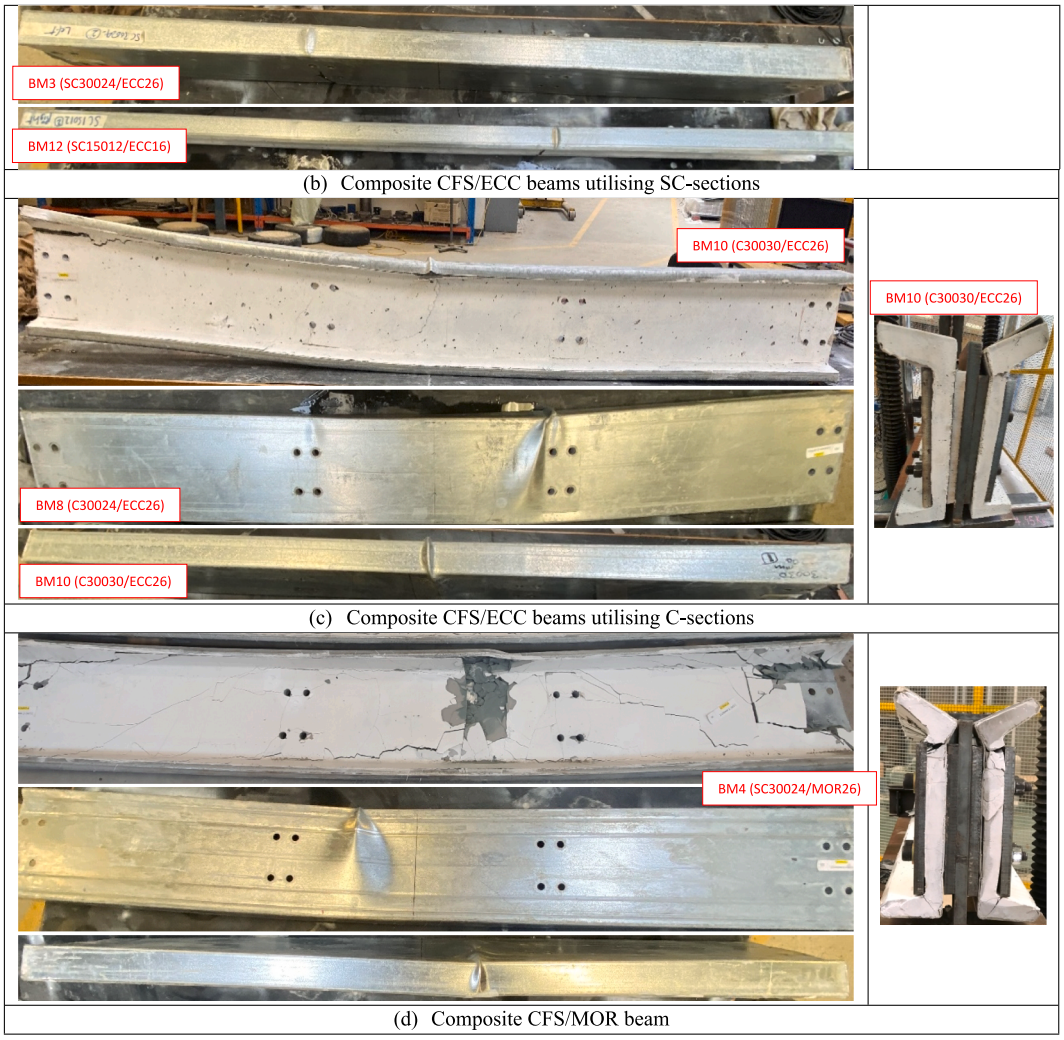

Fig. 16. (*continued*).

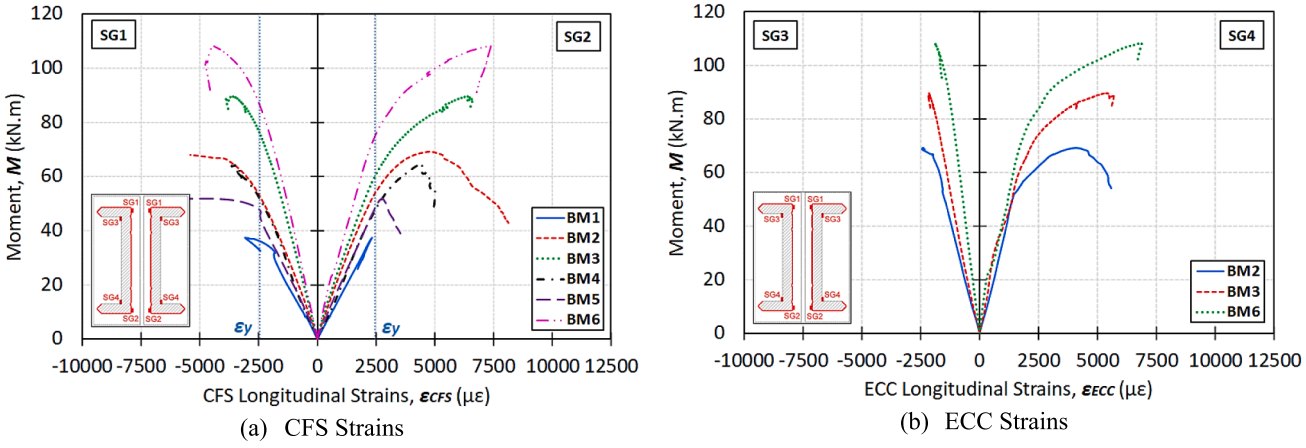

Fig. 17. Longitudinal strains of Series A.

behaviour that was different from the composite sections with fully filled CFS lips and comparable to the behaviour of non-compact steel sections [41].

3.5. *Effect of ECC and CFS thicknesses on the flexural behaviour*

CFS and ECC thicknesses are *two* parameters that significantly influence the flexural behaviour of the composite CFS/ECC beams. Figs. 24 & 25 present the effect of ECC thickness on the moment capacity and flexural toughness, while the effect of CFS thickness is illustrated in

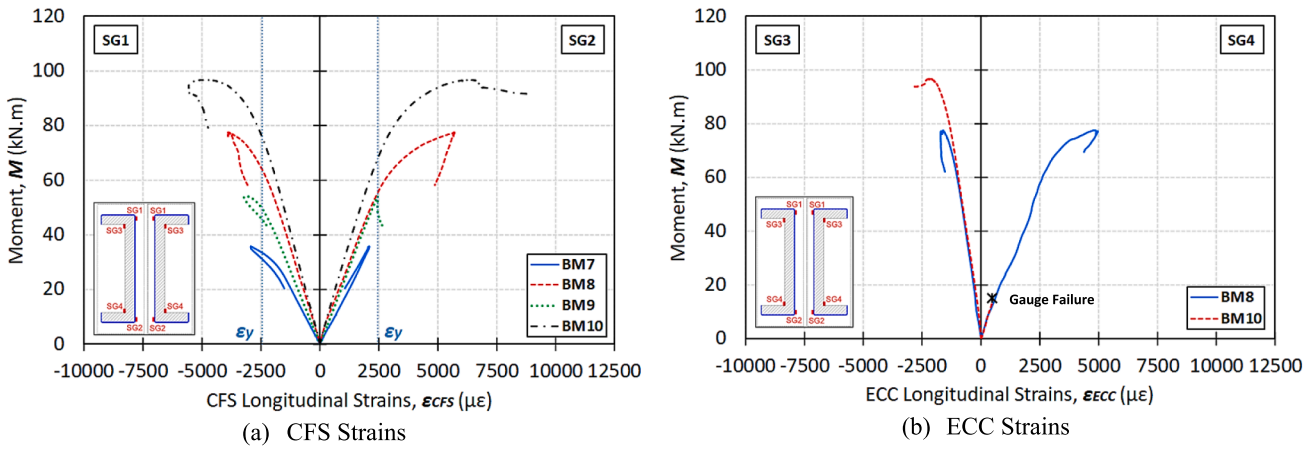

Fig. 18. Longitudinal strains of Series B.

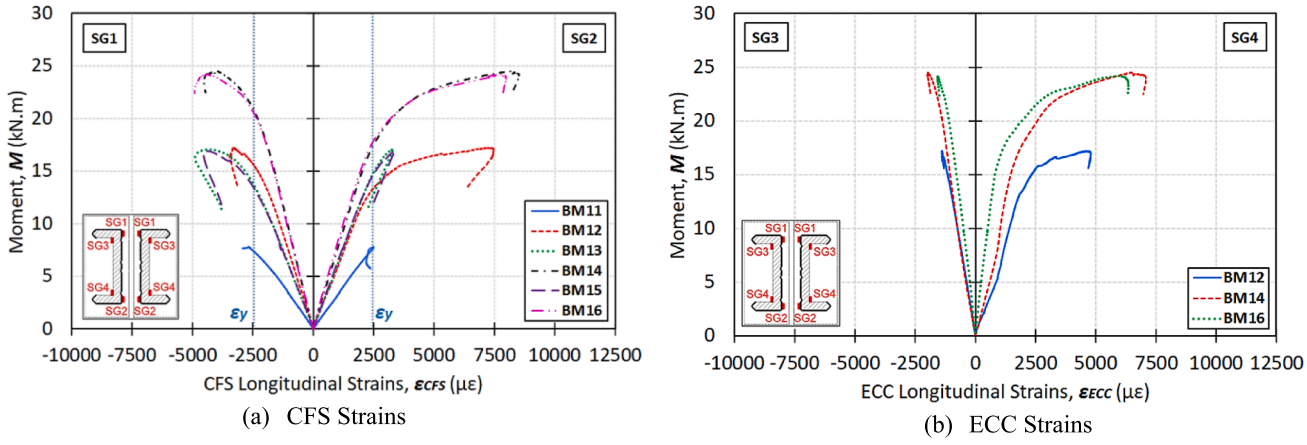

Fig. 19. Longitudinal strains of Series C.

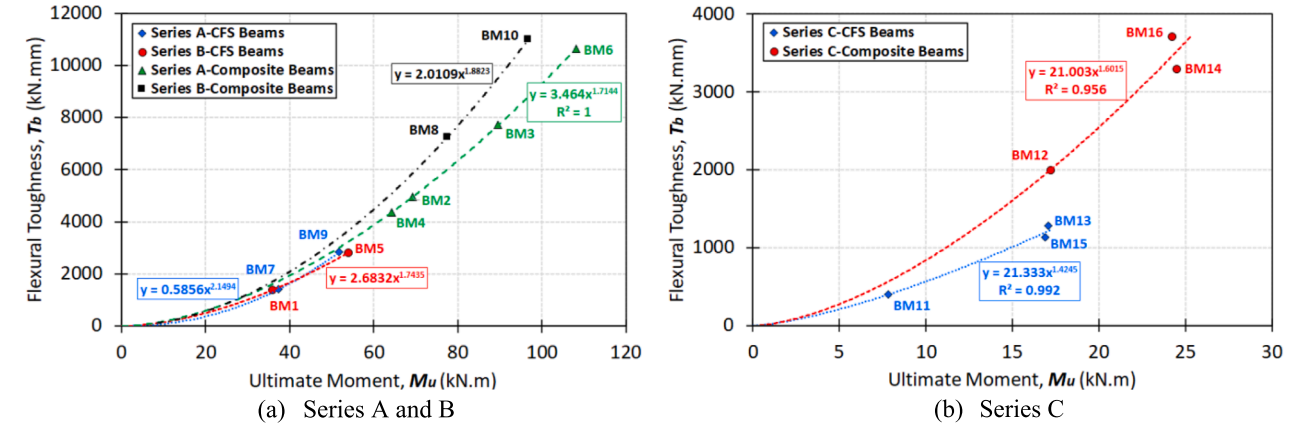

Fig. 20. Flexural toughness (T_b) vs. ultimate moment (M_u).

Figs. 26 & 27. The rate of moment capacity increase with the ECC thickness (limited by CFS lip height) was higher with the SC-sections, with different thicknesses, than the C-sections, due to the confinement of the ECC top and bottom flanges from the curved lips. Moreover, for SC150 sections, the moment increase rate with the ECC thickness was higher with the smaller CFS thickness. The flexural toughness of the CFS/ECC beams increased with the ECC thickness at the same rate for both SC- and C-sections, and it can be seen that the increase rates were higher with the larger SC- and C-section thicknesses.

The effect of CFS thickness (Figs. 26 & 27) was only analysed in the range studied in the experimental study. The growth rates of moment capacity of CFS/ECC beams with the CFS thickness were similar for both SC- and C- beams, unlike the effect of ECC thickness. Furthermore, the flexural toughness increase with the CFS thickness was at a higher rate in the composite beams compared to bare CFS beams.

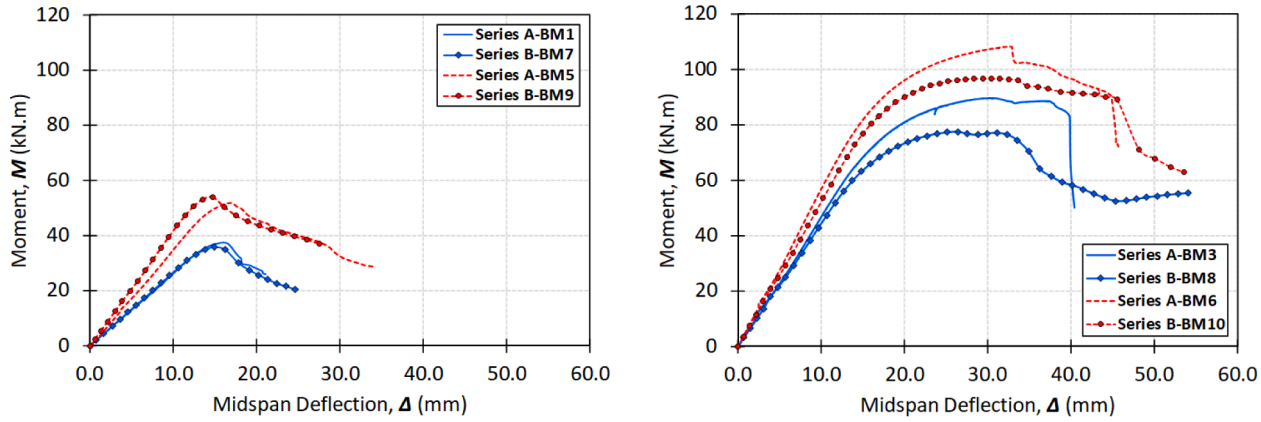

(a) Bare CFS beams (Series A, B) (b) Composite CFS/ECC beams (Series A, B)

Fig. 21. Comparison of moment vs. midspan deflection for Series A and B.

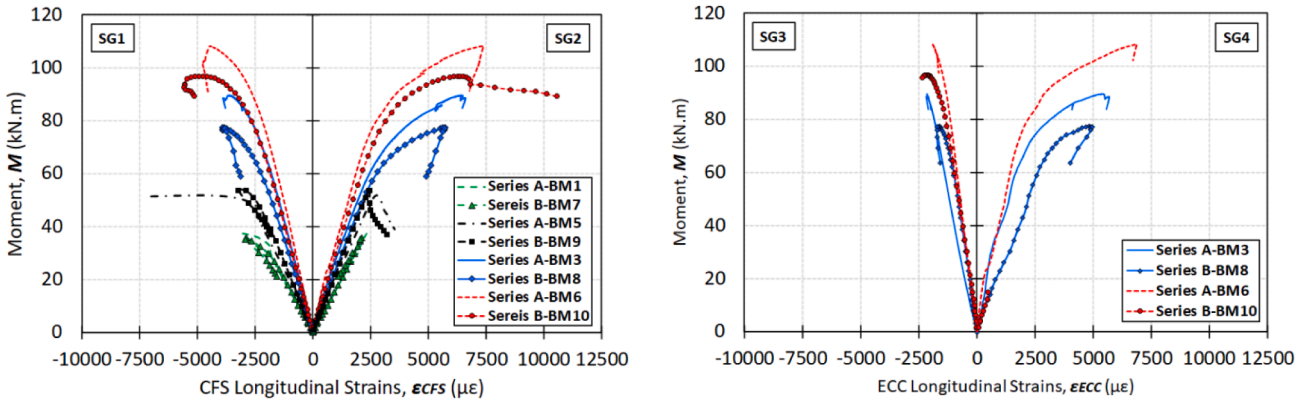

(a) CFS longitudinal strains (Series A, B) (b) ECC longitudinal strains (Series A, B)

Fig. 22. Comparison of longitudinal strains for Series A and B.

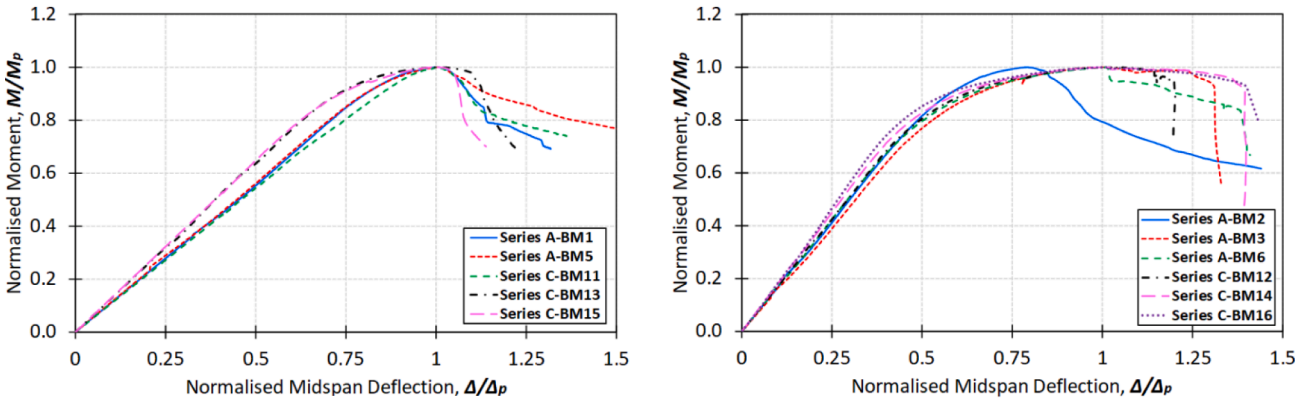

(a) Bare CFS beams (b) Composite CFS/ECC beams

Fig. 23. Normalised moment vs. normalised deflection for Series A and C.

4. Flexural strength prediction

This section presents prediction equations for the moment capacity of the composite CFS/ECC beams. The proposed equations are developed based on the observed ultimate moments, deflections, and failure modes from this experimental study and using the design equations for CFS and hot-rolled steel members subjected to bending in AS/NZS 4600 [42] and AS 4100 [43]. These equations assumed perfect composite action between CFS sections and ECC layers, as no significant end slippage or debonding was observed in the tested CFS/ECC composite beams, until reaching their ultimate moment capacities. However, this assumption is irrelevant for the CFS/MOR beam as debonding between CFS and MOR was observed, after significant cracking and crushing of the MOR layer, before reaching the ultimate moment.

The composite CFS/ECC sections can be classified according to their slenderness as compact (C), non-compact (NC), and slender (S) sections.

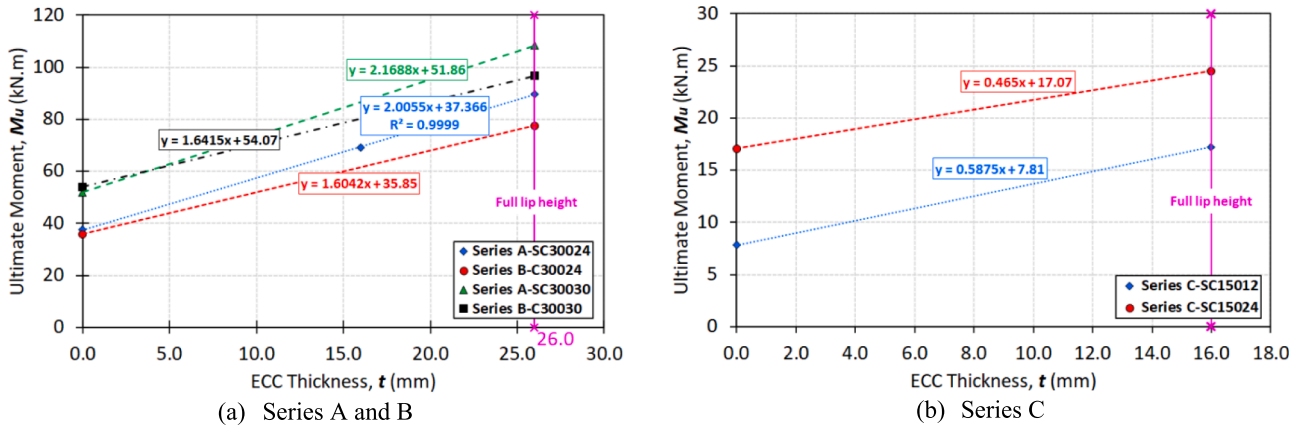

Fig. 24. Effect of ECC thickness *(t)* on the moment capacity.

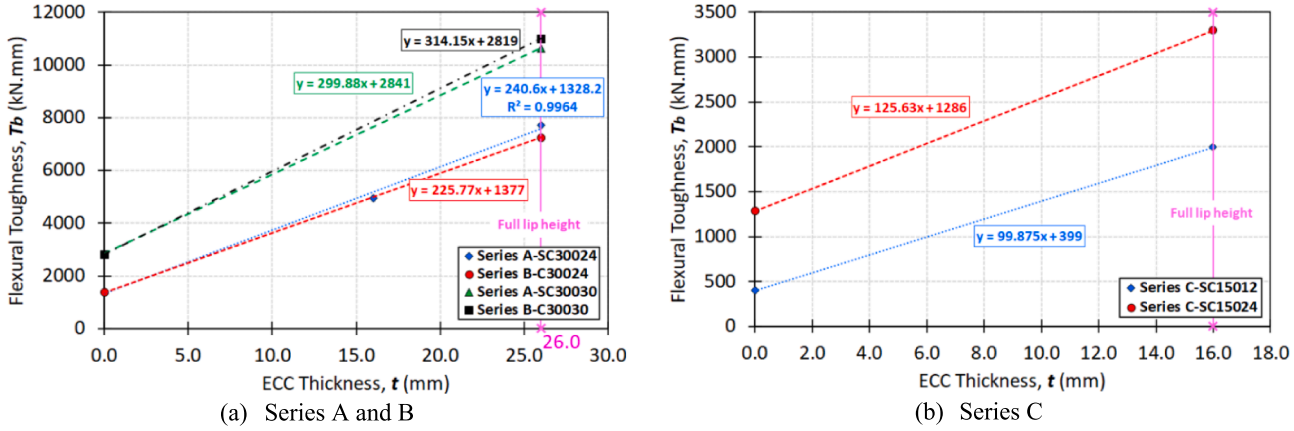

Fig. 25. Effect of ECC thickness, *(t)* on the flexural toughness.

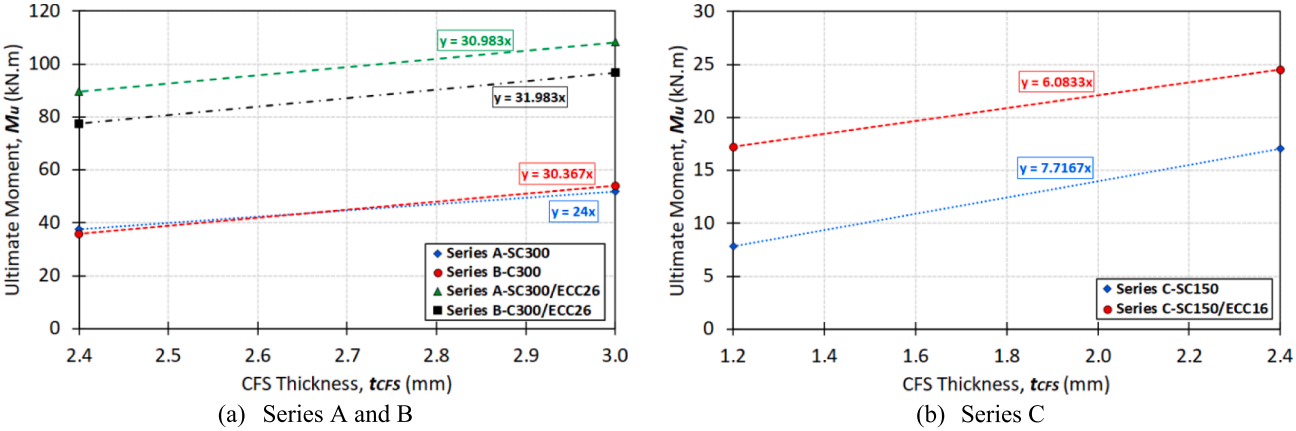

Fig. 26. Effect of CFS thickness *(t_{CFS})* on the moment capacity.

The slenderness ratio (λ_c) of the composite CFS/ECC sections is determined using **Equation (1)**, similar to hot-rolled steel sections [43]. In the slenderness ratio calculations, b_c is the clear width of the compression flange of the composite section, where t_{eq} is the equivalent steel thickness of the composite section (calculated using the modular ratio, $n = E_{CFS}/E_{ECC}$). The section moment capacity of composite CFS/ECC beams (M_{cs}) can be predicted according to their slenderness ratios (λ_c) using **Equations (2–4)**. For compact CFS/ECC composite sections, the moment capacity is their plastic moment capacity (M_{cp}), while the non-compact sections have capacity between their yield and plastic section moment capacities (M_{cy} & M_{cp}). Additionally, the moment capacity of the slender sections is less than their yield moment capacities (M_{cy}).

$$\lambda_c = \frac{b_c}{t_{eq}}\sqrt{\frac{f_y}{250}} \tag{1}$$

For $\lambda_c < \lambda_{cp}$: section is **Compact (C)**,.$M_{cs} \geq M_{cp}$

$$M_{cs} = M_{cp} \tag{2}$$

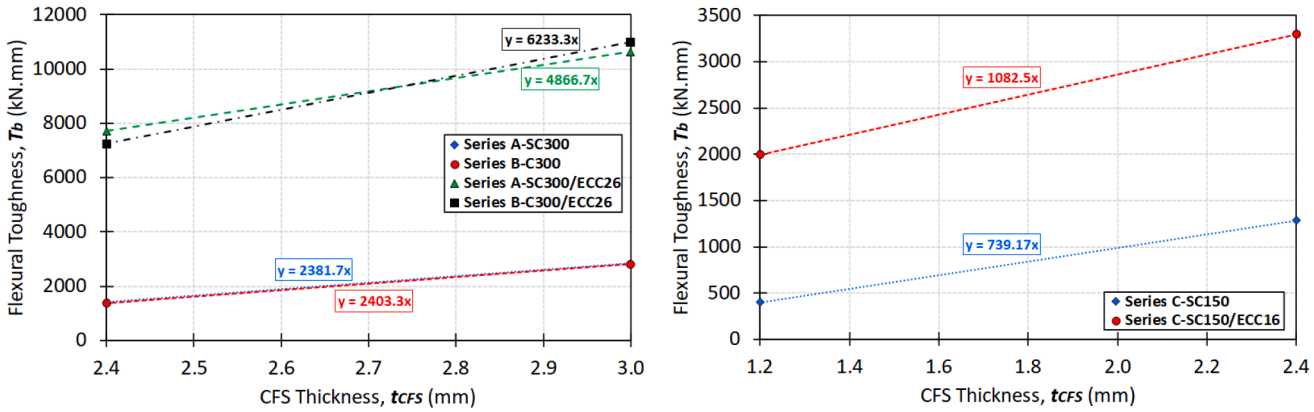

(a) Series A and B (b) Series C

Fig. 27. Effect of CFS thickness (t_{CFS}) on the flexural toughness.

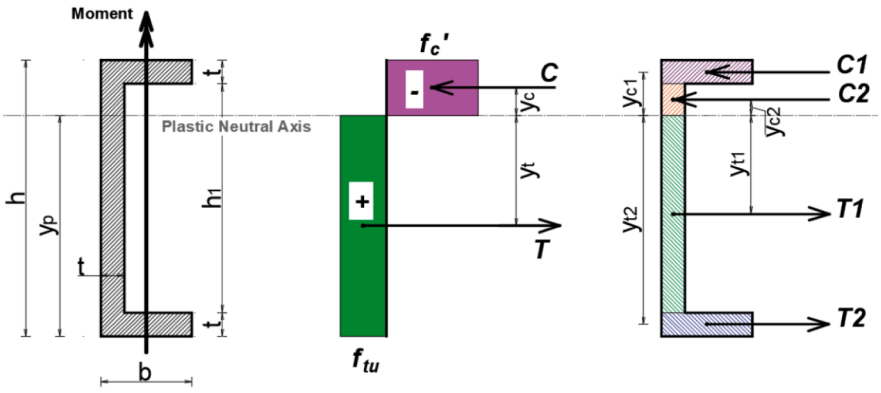

(a) Cross-section of ECC layer (b) Stress distribution of fully plastic ECC section (c) Plastic moment analysis

Fig. 28. Plastic moment capacity of the ECC section.

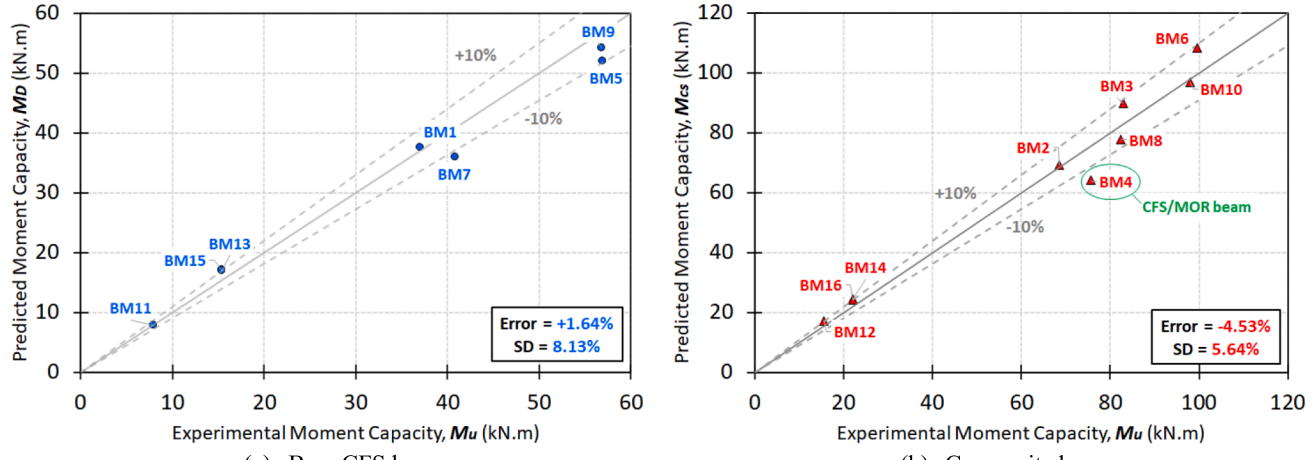

(a) Bare CFS beams (b) Composite beams

Fig. 29. Accuracy of the flexural strength prediction equations.

For $\lambda_{cy} < \lambda_c < \lambda_{cp}$: section is **Non-compact (NC)**,.$M_{cy} \le M_{cs} < M_{cp}$

$$M_{cs} = M_{cy} + \left[\left(\frac{\lambda_{cy} - \lambda_c}{\lambda_{cy} - \lambda_{cp}}\right)(M_{cp} - M_{cy})\right] \quad (3)$$

For $\lambda_c > \lambda_{cy}$: section is **Slender (S)**,.$M_{cs} > M_{cy}$

$$M_{cs} = \frac{\lambda_c}{\lambda_{cy}} M_{cy} \quad (4)$$

The section moment capacity (M_{cs}) for a non-compact composite section in **Equation (3)** is calculated based on interpolation between the yield and plastic section moment capacities (M_{cy} & M_{cp}), similar to non-

Table 7
Predicted and experimental moment capacities of the bare CFS beams.

Series	Beam Specimen	Beam Code	Strength Prediction				Experimental Results	Equation Accuracy	
			Predicted Capacity [AS/NZS 4600]						
			Section Moment Capacity, M_s [kN.m]	Member Moment Capacity, M_b [kN.m]	Theoretical Governing Failure Mode	Design Moment Capacity, M_D [kN.m]	Ultimate Moment Capacity, M_u [kN.m]	M_D/M_u [%]	Error [%]
Series A [SC300]	*SC30024*	*BM1*	*50.23*	*37.06*	***Distortional Buckling***	***37.06***	***37.46***	*98.93*	*−1.07*
	SC30030	*BM5*	*65.22*	*56.92*	***Distortional Buckling***	***56.92***	***51.86***	*109.76*	*+9.76*
Series B [C300]	*C30024*	*BM7*	*44.64*	*40.83*	***Distortional Buckling***	***40.83***	***35.85***	*113.90*	*+13.90*
	C30030	*BM9*	*60.76*	*56.82*	***Distortional Buckling***	***56.82***	***54.07***	*105.08*	*+5.08*
Series C [SC150]	*SC15012*	*BM11*	*9.36*	*7.95*	***Distortional Buckling***	***7.95***	***7.81***	*101.79*	*+1.79*
	SC15024	*BM13*	*16.37*	*15.46*	***Distortional Buckling***	***15.46***	***17.07***	*90.57*	*−9.43*
	*SC15024-**S***	*BM15*	*16.37*	*15.46*	***Distortional Buckling***	***15.46***	***16.91***	*91.43*	*−8.57*
Mean								***101.64%***	***+1.64%***
SD								***8.13%***	

Table 8
Predicted and experimental moment capacities of the composite beams.

Series	Beam Specimen	Beam Code	Strength Prediction					Experimental Results	Equation Accuracy	
			Section Classification		Predicted Capacity					
			Slenderness Ratio, λ_e	Compactness	Yield Moment Capacity, M_{cy} [kN.m]	Plastic Moment Capacity, M_{cp} [kN.m]	Section Moment Capacity, M_{cs} [kN.m]	Ultimate Moment Capacity, M_u [kN.m]	M_{cs}/M_u [%]	Error [%]
Series A [SC300]	*SC30024-**ECC16***	*BM2*	*11.00*	***Non-Compact (NC)***	*57.77*	*76.62*	***68.54***	***69.21***	*99.03*	*−0.97*
	*SC30024-**ECC26***	*BM3*	*6.83*	***Compact (C)***	*58.73*	*83.05*	***83.05***	***89.66***	*92.63*	*−7.37*
	*SC30024-**MOR26***	*BM4*	*5.68*	***Compact (C)***	*58.72*	*75.70*	***75.70***	***64.28***	*117.77*[f]	*+17.77*[f]
	*SC30030-**ECC26***	*BM6*	*6.67*	***Compact (C)***	*72.74*	*99.59*	***99.59***	***108.25***	*92.00*	*−8.00*
Series B [C300]	*C30024-**ECC26***	*BM8*	*6.58*	***Compact (C)***	*58.41*	*82.49*	***82.49***	***77.56***	*106.36*	*+6.36*
	*C30030-**ECC26***	*BM10*	*6.31*	***Compact (C)***	*72.88*	*99.12*	***98.11***	***96.75***	*101.41*	*+1.41*
Series C [SC150]	*SC15012-**ECC16***	*BM12*	*8.18*	***Compact (C)***	*11.02*	*15.51*	***15.51***	***17.21***	*90.12*	*−9.88*
	*SC15024-**ECC16***	*BM14*	*6.49*	***Compact (C)***	*16.90*	*22.19*	***22.19***	***24.51***	*90.53*	*−9.47*
	*SC15024-**ECC16-S***	*BM16*	*6.49*	***Compact (C)***	*16.90*	*22.19*	***22.19***	***24.21***	*91.66*	*−8.34*
Mean									***95.47%***	***−4.53%***
SD									***5.64%***	

[f] Not included in the mean and SD values (**BM4** is **CFS/MORbeam**).

compact hot-rolled steel sections [43]. The slenderness yield and plastic limits (λ_{cy} & λ_{cp}) for the composite sections can be taken as *15* and *8*, respectively, similar to hot-rolled steel sections with compression flanges longitudinally supported from one edge [43].

The yield moment capacity of composite sections (M_{cy}) can be determined based on the yielding of the CFS section and the initial cracking of the ECC layer in tension using **Equations (5 & 6)** [44]. The plastic moment capacity of composite sections (M_{cp}) can be calculated using **Equations (7 & 8)**, assuming both the CFS section and the ECC layer achieved their plastic moment capacities based on the experimental observations. The plastic moment of the CFS section is calculated as $Z_p f_y$, where Z_p is the plastic section modulus and f_y is the yield strength of CFS [44]. For the ECC layer, the plastic moment capacity can be determined using plastic analysis [44,45] as shown in Fig. 28, where C and T are the total equivalent compressive and tensile forces of the fully plastic section. To simplify the plastic moment calculations for the ECC section ($M_{p,ECC}$), the plastic neutral axis was assumed at the bottom edge of the compression flange ($C_2 \approx 0.0$). (SEE Fig. 29.).

$$M_{cy} = M_{y,CFS} + M_{cr,ECC} \tag{5}$$

$$M_{cy} = \left[Z_f f_y\right] + \left[f_t \frac{I_g}{y_t}\right] \tag{6}$$

$$M_{cp} = M_{p,CFS} + M_{p,ECC} \tag{7}$$

$$M_{cp} = \left[Z_n f_y\right] + \left[0.5bt^2 f_c^{'} + 0.5h_1^2 t f_{tu} + bt(h_1 + 0.5t) f_{tu}\right] \quad (8)$$

The bare CFS beams were susceptible to distortional buckling as the compression and tension flanges were free to move laterally. The moment capacity of CFS beams (M_D) can be defined, according to AS/NZS 4600 [42], as the lesser value of the nominal section moment capacity (M_s) and the nominal member moment capacity (M_b). The section moment capacity (M_s) is determined per AS/NZS 4600 [42], based on the inception of yielding in the compression flange (local buckling) using **Equation (9)**. The member moment capacity (M_b) of the CFS sections subject to distortional buckling can be calculated using **Equation (10)** per AS/NZS 4600 [42].

$$M_s = Z_e f_y \quad (9)$$

$$M_b = Z_c f_c \quad (10)$$

where:

$$f_c = M_c/Z_f,\ M_c = \left\{ \begin{array}{c} M_y for \lambda_d \le 0.674 \\ M_y/\lambda_d(1 - 0.22/\lambda_d) for \lambda_d > 0.674 \end{array} \right\},\ M_y = Z_f f_y, .\lambda_d = \sqrt{M_y/M_{od}}$$

The predicted and experimental moment capacities for the bare CFS and composite beams are compared in Tables 7, 8 and Fig. 28. The accuracy of the estimated moment capacities of the bare CFS beams (M_D/M_u), calculated as per AS/NZS 4600 design equations [42], was 101.64% with an average error of 1.64% and standard deviation (*SD*) of 8.13%. The developed prediction equations for the moment capacities of composite CFS/ECC beams showed an average accuracy (M_{cs}/M_u) of 95.47%, with an error of −4.53% and *SD* of 5.64%. The predicted capacity of the composite CFS/MOR beam (BM4) was excluded from the mean value and standard deviation of the prediction equation accuracy due to debonding between MOR and CFS after significant cracking and crushing of the MOR layer. When including the capacity of the composite CFS/MOR beam, the prediction equations accuracy would be 97.95% with an average error of −2.05% and *SD* of 8.80%.

5. Conclusions and future work

This research presents a conceptual investigation on the flexural behaviour of novel thin-walled composite CFS/ECC beams through detailed experimental study. The composite system reduced the buckling issues associated with the CFS flexural members, leading to higher moment capacities and flexural toughness. This study comprises *three* series of large-scale simply supported composite and bare CFS beams tested under a *4*-point loading configuration. SupaCee (SC) and lipped-Cee (C) sections with different sizes and thicknesses were employed with PE-ECC in the composite sections. High-strength mortar (MOR) was utilised in *one* composite beam for comparison with the composite beams incorporating PE-ECC. From the experimental and analytical study, it can be summarised that:

- Bare CFS beams failed due to distortional buckling and could not reach their yield moment capacity (section capacity). However, composite CFS/ECC beams, with ECC filling the full lip height of CFS sections, reached their plastic moment capacities and failed due to local buckling of the CFS top flange and crushing of ECC top flange, followed by rupture of the ECC and CFS bottom flanges. Composite CFS/MOR beam, with the MOR layer filling the full CFS lip height, could not reach the plastic moment capacity due to debonding between MOR and CFS after MOR crushing.
- The moment capacities of composite CFS/ECC beams, incorporating SC300 sections with ECC filling *100.0%* of lip height, were *208.73* to *239.35%* of their bare CFS sections, and with ECC filling *60.0%* of lip height, the moment capacity was *184.75%* of the bare CFS. The ultimate moment of the CFS/MOR beam was *171.59%* of the bare CFS, indicating that PE-ECC was more effective than MOR in the composite beams. Moreover, the moment capacities of composite beams using SC150 sections, with ECC filling total lip height, were *143.58* to *220.36%* of the bare CFS sections. The ultimate moments of CFS/ECC beams utilising, C300 sections and ECC filling full lip height, were *178.93* to *216.34%* of their bare CFS. The higher moment capacities of composite beams incorporating SC-sections over C-sections were due to the confinement of ECC flanges from curved lips of the CFS section.
- The flexural toughness of the CFS/ECC beams, utilising *2.4-mm* thick SC300 and C300 sections, were *5.26–5.47* times those of the bare CFS sections, while for the CFS/ECC beams, utilising *3.0-mm* thick SC300 and C300 sections, were *3.74–3.90* times those of the bare sections. Besides, the CFS/MOR beam, utilising a *2.4-mm* thick SC-section, exhibited flexural toughness *3.08* times that of the bare CFS beam.
- Strength prediction equations were developed using AS/NZS 4600 and AS 4100 to estimate the ultimate moment capacity of the composite CFS/ECC beams according to their slenderness ratios (λ_c). The predicted moment capacities of the CFS/ECC beams showed good agreement with the experimental results with an error of −4.53% and standard deviation (*SD*) of 5.64%.
- While the experimental results indicate the potential of the proposed structural concept, more future research work is required to fully capture the performance of the innovated system.

- To conduct case study for practical applications of the proposed structural system.
- To study the cracking development and the interfacial bond behaviour between the CFS sections and PE-ECC layers.
- To investigate the long-term effect on the composite action and flexural behaviour of the composite CFS/ECC beams.
- To conduct detailed computational study for better understanding of the structural performance of the innovated structural concept.

Declaration of Competing Interest

The authors declare that they have no known competing financial interests or personal relationships that could have appeared to influence the work reported in this paper.

References

[1] Keerthan P, Mahendran M. Experimental investigation and design of lipped channel beams in shear. Thin-Walled Struct 2015;86:174–84.
[2] Pham CH, Hancock GJ. Experimental investigation and direct strength design of high-strength, complex C-sections in pure bending. J Struct Eng 2013;139:1842–52.
[3] Ma W, Becque J, Hajirasouliha I, Ye J. Cross-sectional optimization of cold-formed steel channels to Eurocode 3. Eng Struct 2015;101:641–51.
[4] Mojtabaei SM, Ye J, Hajirasouliha I. Development of optimum cold-formed steel beams for serviceability and ultimate limit states using Big Bang-Big Crunch optimisation. Eng Struct 2019;195:172–81.
[5] Ye J, Becque J, Hajirasouliha I, Mojtabaei SM, Lim JBP. Development of optimum cold-formed steel sections for maximum energy dissipation in uniaxial bending. Eng Struct 2018;161:55–67.
[6] Li VC. Engineered cementitious composites tailored composites through micromechanical modeling, fiber reinforced concrete: present and the future. CSCE 1998:64–97.
[7] Li VC, Wu C, Wang S, Ogawa A, Saito T. Interface tailoring for strain-hardening polyvinyl alcohol-engineered cementitious composite (PVA-ECC). ACI Mater J 2002;99:463–72.
[8] Yu K, Wang Y, Yu J, Xu S. A strain-hardening cementitious composites with the tensile capacity up to 8%. Constr Build Mater 2017;137:410–9.
[9] Li VC. Tailoring ECC for special attributes: a review. Int J Concre Struct Mater 2012;6:135–44.
[10] Zhou S, Rabczuk T, Zhuang X. Phase field modeling of quasi-static and dynamic crack propagation: COMSOL implementation and case studies. Adv Eng Softw 2018;122:31–49.
[11] Hamdia KM, Silani M, Zhuang X, He P, Rabczuk T. Stochastic analysis of the fracture toughness of polymeric nanoparticle composites using polynomial chaos expansions. Int J Fract 2017;206:215–27.
[12] Qian S, Li VC. Simplified inverse method for determining the tensile strain capacity of strain hardening cementitious composites. J Adv Concr Technol 2007;5:235–46.
[13] Uy B, Mendis P, Ngo T. In: Modern design, construction and maintenance of composite steel-concrete structures: Australian experiences. Construction Publishing House; 2007. p. 151–8.

[14] Liang QQ, Uy B, Bradford MA, Ronagh HR. Strength analysis of steel-concrete composite beams in combined bending and shear. J Struct Eng 2005;131:1593–600.
[15] Oehlers JD. Composite Profiled beams. J Struct Eng 1993;119:1085–100.
[16] Thin-Walled NP, Beams C-F. J Struct Eng 1991;117:2936–52.
[17] Wehbe N, Bahmani P, Wehbe A. Behavior of concrete/cold formed steel composite beams: experimental development of a novel structural system. Int J Concr Struct Mater 2013;7:51–9.
[18] Rana MM, Lee CK, Al-Deen S, Zhang YX. Flexural behaviour of steel composite beams encased by engineered cementitious composites. J Constr Steel Res 2018;143:279–90.
[19] De Nardin S, El Debs ALHC. Study of partially encased composite beams with innovative position of stud bolts. J Constr Steel Res 2009;65:342–50.
[20] Abdel-Sayed G. Composite cold-formed steel-concrete beams. J Struct Div 1982;108:2609–22.
[21] Kabir MI, Lee CK, Rana MM, Zhang YX. Flexural and bond-slip behaviours of engineered cementitious composites encased steel composite beams. J Constr Steel Res 2019;157:229–44.
[22] Kabir MI, Lee CK, Rana MM, Zhang YX. Strength enhancement of high strength steel beams by engineered cementitious composites encasement. Eng Struct 2020;207:110288.
[23] Kabir MI, Lee CK, Rana MM, Zhang YX. Flexural behaviour of ECC-LWC encased slender high strength steel composite beams. J Constr Steel Res 2020;173:106253.
[24] Sheta A, Ma X, Zhuge Y, ElGawady MA, Mills JE, Singh A, et al. Structural performance of novel thin-walled composite cold-formed steel/PE-ECC beams. Thin-Walled Structures 2021;162.
[25] LYSAGHT. SUPAPURLINS SUPAZEDS & SUPACEES Design and Installation Guide for Building Professionals. In: Steel B, editor. Sydney, Australia: LYSAGHT; 2017.
[26] LYSAGHT. ZEDS and CEES User Guide for Design and Installation Professionals. In: Steel B, editor. Sydney, Australia: LYSAGHT; 2017.
[27] Ye J, Mojtabaei SM, Hajirasouliha I. Local-flexural interactive buckling of standard and optimised cold-formed steel columns. J Constr Steel Res 2018;144:106–18.
[28] Ye J, Mojtabaei SM, Hajirasouliha I, Shepherd P, Pilakoutas K. Strength and deflection behaviour of cold-formed steel back-to-back channels. Eng Struct 2018;177:641–54.
[29] ASTM E8. Standard test methods for tension testing of metallic materials. Annual book of ASTM standards ASTM. 2001.
[30] Standards Australia. Supplementary cementitious materials, Part 3: Amorphous silica, AS/NZS 3582.3. AS/NZS 35823. Australia: Standards Australia; 2016.
[31] Standards Australia. General purpose and blended cements, AS 3972. AS 3972-2010. Australia: Standards Australia; 2010.
[32] Standards Australia. Supplementary cementitious materials, Part 2: Slag - Ground granulated blast-furnace, AS 3582.2. AS 35822. Australia: Standards Australia; 2016.
[33] Ding Y, Yu J-t, Yu K-Q, Xu S-l. Basic mechanical properties of ultra-high ductility cementitious composites: From 40 MPa to 120 MPa. Compos Struct 2018;185:634–45.
[34] Yu K-Q, Yu J-T, Dai J-G, Lu Z-D, Shah SP. Development of ultra-high performance engineered cementitious composites using polyethylene (PE) fibers. Constr Build Mater 2018;158:217–27.
[35] Yang E-H, Mustafa Sahmaran YY, Victor CL. Rheological control in production of engineered cementitious composites. ACI Mater J 2009;106.
[36] Wang Y, Liu F, Yu J, Dong F, Ye J. Effect of polyethylene fiber content on physical and mechanical properties of engineered cementitious composites. Constr Build Mater 2020;251:118917.
[37] Rabczuk T, Belytschko T. Cracking particles: a simplified meshfree method for arbitrary evolving cracks. Int J Numer Meth Eng 2004;61:2316–43.
[38] Rabczuk T, Belytschko T. A three-dimensional large deformation meshfree method for arbitrary evolving cracks. Comput Methods Appl Mech Eng 2007;196:2777–99.
[39] Mahendran M, Keerthan P. Experimental studies of the shear behavior and strength of LiteSteel beams with stiffened web openings. Eng Struct 2013;49:840–54.
[40] Turk K, Nehdi ML. Flexural toughness of sustainable ECC with high-volume substitution of cement and silica sand. Constr Build Mater 2021;270:121438.
[41] Ungureanu V, Kotełko M, Karmazyn A, Dubina D. Plastic mechanisms of thin-walled cold-formed steel members in eccentric compression. Thin-Walled Structures 2018;128:184–92.
[42] Standards Australia. Cold-formed steel structures, AS/NZS 4600. AS/NZS 4600-2018. Australia: Standards Australia; 2018.
[43] Standards Australia. Steel Structures, AS 4100. AS 4100-98. Australia: Standards Australia; 1998.
[44] Wong MB. Chapter 2 - Plastic Behavior of Structures. In: Wong MB, editor. Plastic Analysis and Design of Steel Structures. Boston: Butterworth-Heinemann; 2009. p. 55–80.
[45] Neal BG. The plastic methods of structural analysis. Wiley 1963.